Institute of Environmental Physics
University of Bremen

Evaluation of Algorithms for Retrieval of Rain Rate with Passive Microwave Radiometers

with emphasis on

Effects of Spatial and Temporal Sampling

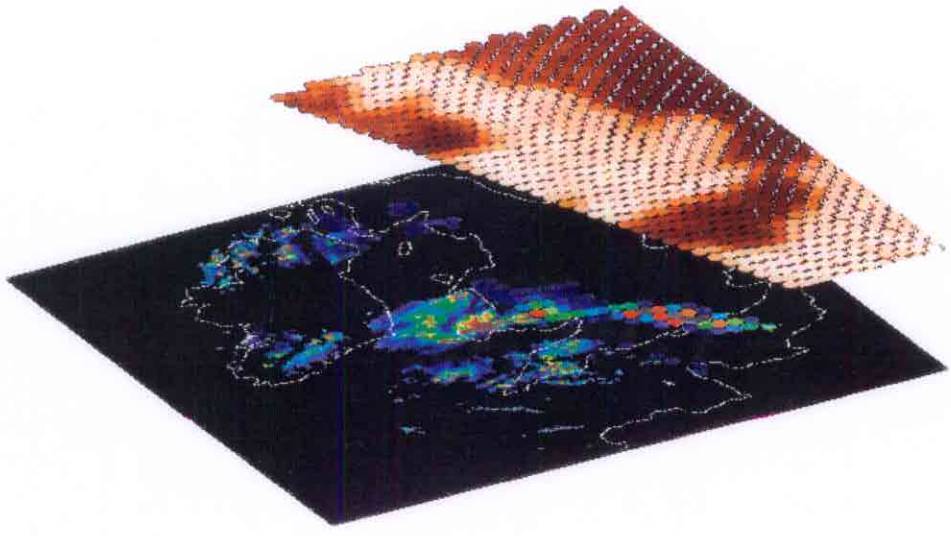

EXECUTIVE SUMMARY

ESTEC Contract 10347/93/NL/NB(SC)

August 1994

Final Report for the European Space Agency
under ESTEC Contract 10347/93/NL/NB(SC)

Evaluation of Algorithms for Retrieval of Rain Rate with Passive Microwave Radiometers

with emphasis on

Effects of Spatial and Temporal Sampling

EXECUTIVE SUMMARY

August 1994

UNIVERSITY OF BREMEN
INSTITUTE OF ENVIRONMENTAL PHYSICS

B. A. Burns, F. Flender, T. Hunewinkel, G. Heygster, K. Künzi

ESA Technical Management: J. P. V. Baptista

Preface

The project "Evaluation of Algorithms for Retrieval of Rain Rate with Passive Microwave Radiometers" has been carried out by the University of Bremen for the European Space Agency. Three investigations have been completed under this project:

1. review, implementation, and evaluation of algorithms for rain retrieval over land;

2. analysis of the spatial and temporal sampling problem including beam-filling effects for the SSM/I and MIMR instruments, its impact on rainfall retrieval and possible solutions; and

3. review and comparison of image restoration algorithms for resolution improvement.

This Executive Summary presents the results of these investigations in the form of two papers to be published in the *ESA Journal*. The first paper "Rain Retrieval over Land with Passive Microwave Satellite Sensors: Errors due to Surface Variation and Sensor Sampling Characteristics" summarizes the results obtained in the first two investigations. The second paper summarizes the work done under the third investigation and is entitled "Image Restoration Techniques for Improving SSM/I Spatial Resolution".

Contents

Part 1

Rain Retrieval over Land with Passive Microwave Satellite Sensors: Errors due to Surface Variation and Sensor Sampling Characteristics

Introduction

Algorithms for the retrieval of rain rate using Passive Microwave Imagers (PMI) have been investigated in a previous ESA-supported study [Burns *et al.*, 1993]. In that study presently available algorithms were reviewed with emphasis on how the higher frequency (37 and 85 GHz) channels were incorporated into the rain retrieval. Several algorithms were then implemented and applied to model-generated data for precipitating clouds in order to evaluate the effect of water vapor and cloud liquid water variations on rain rate retrievals. It was found that most algorithms still depend heavily on the 19 GHz channels which sense the vertically integrated water content. Many algorithms make use of the 85 GHz channel for correction of the effects of ice particle scattering, but little use has been made so far of its higher resolution. The algorithms implemented showed very little sensitivity (< 1 mm/hr change) to the atmospheric variations mainly because they had been calibrated with model or observational data for rain cloud characteristics different from those used to generate brightness temperature data in this study. However the large brightness temperature difference found between rain and no-rain clouds or clear air at 37 and 85 GHz (as much as $\pm$20K) indicated that rain detection and retrieval for areas of rain cloud much smaller than the PMI footprint (FOV) would be prone to large errors if variations in atmospheric conditions are not accounted for. It was suggested that a more meaningful evaluation would require simulation of radiometer measurements where rain cells only partially fill the FOV.

Most of the algorithms investigated in the previous study were for rain retrieval over the ocean. Rain measurement over land is more difficult because, in contrast to the low background emissivity of the ocean, the emissivity of land is not only

generally high but also highly variable. This is illustrated in Figure 1.1 which shows model data for ocean and land backgrounds. Brightness temperature contrasts between nonprecipitating clouds with varying liquid water contents is greatest over the ocean where the emission from the atmosphere constitutes a large fraction of the total signal. Over land brightness temperatures are dominated by the contribution from the surface and little difference between clear air and thin clouds is seen. On the other hand, optically thick rain clouds show distinct signatures and for these cases rain retrievals with the same algorithm over land and ocean should be possible (see also [Smith *et al.*, 1992]).

This presumes that rain areas can first of all be detected, which is hindered by the nonuniformity of the land surface. Variations in soil moisture, soil type, vegetation, ice and snow cover lead to variations in brightness temperature that are similar in magnitude and spatial scale to those caused by rain clouds themselves. At 19 GHz soil moisture variability alone leads to brightness temperature contrasts larger than that between clear air and the stratiform rain cloud shown in Figure 1.1. At 85 GHz, however, emissivity variability is reduced and sensitivity to rain increased, meaning better detection potential at the higher frequencies.

One goal of this investigation is the review, implementation and evaluation of algorithms for rain retrievals over land. Algorithms reviewed are mainly those considered under the AIP-2 and PIP-1 algorithm intercomparison projects [Allam *et al.*, 1993; Kniveton *et al.*, 1994]. A subset of these algorithms are evaluated for their sensitivity to variations in land emissivity and temperature. For this purpose model generated brightness temperature data are used. These same algorithms are applied to the SSM/I data from the AIP-2 data set and a statistical analysis of their performance is carried out.

Part of the difficulty in determining relative algorithm performance lies in the nature of the retrieval error itself, which is contributed to by both the inadequacy of algorithm formulation to represent the actual Tb-RR relationship and the deviation of surface and atmospheric conditions from those used to develop the algorithm. The first factor is essentially what should be determined through intercomparison and validation. However because different algorithms are generally calibrated with different data sets, and not necessarily with data sets representative of the area of interest, the second factor can be responsible for major algorithm-to-algorithm variations. A recalibration of the algorithms with the AIP-2 data set is therefore carried out in this study.

Additional errors in both algorithm validation and in the retrievals themselves can result from the spatial and temporal sampling characteristics of PMI sensors. Because rain fields and clouds can be patchy on scales much smaller than the footprint of the passive microwave imager, errors are introduced when only part of the FOV contains rain (cloud). This is called the beam-filling error, and errors as large as 50% have been observed [Short and North, 1990]. The magnitude of this error is understandable when one considers the large brightness temperature variability possible within a pixel encompassing clear air, precipitating and nonprecipitating cloud areas (see model data in Figure 1.1). And for rain systems with core sizes of 1-2 km [Goldhirsh and Musiani, 1992] this is a typical situation. Furthermore rain retrieval is based on a "mean" brightness temperature for the pixel that is not a sim-

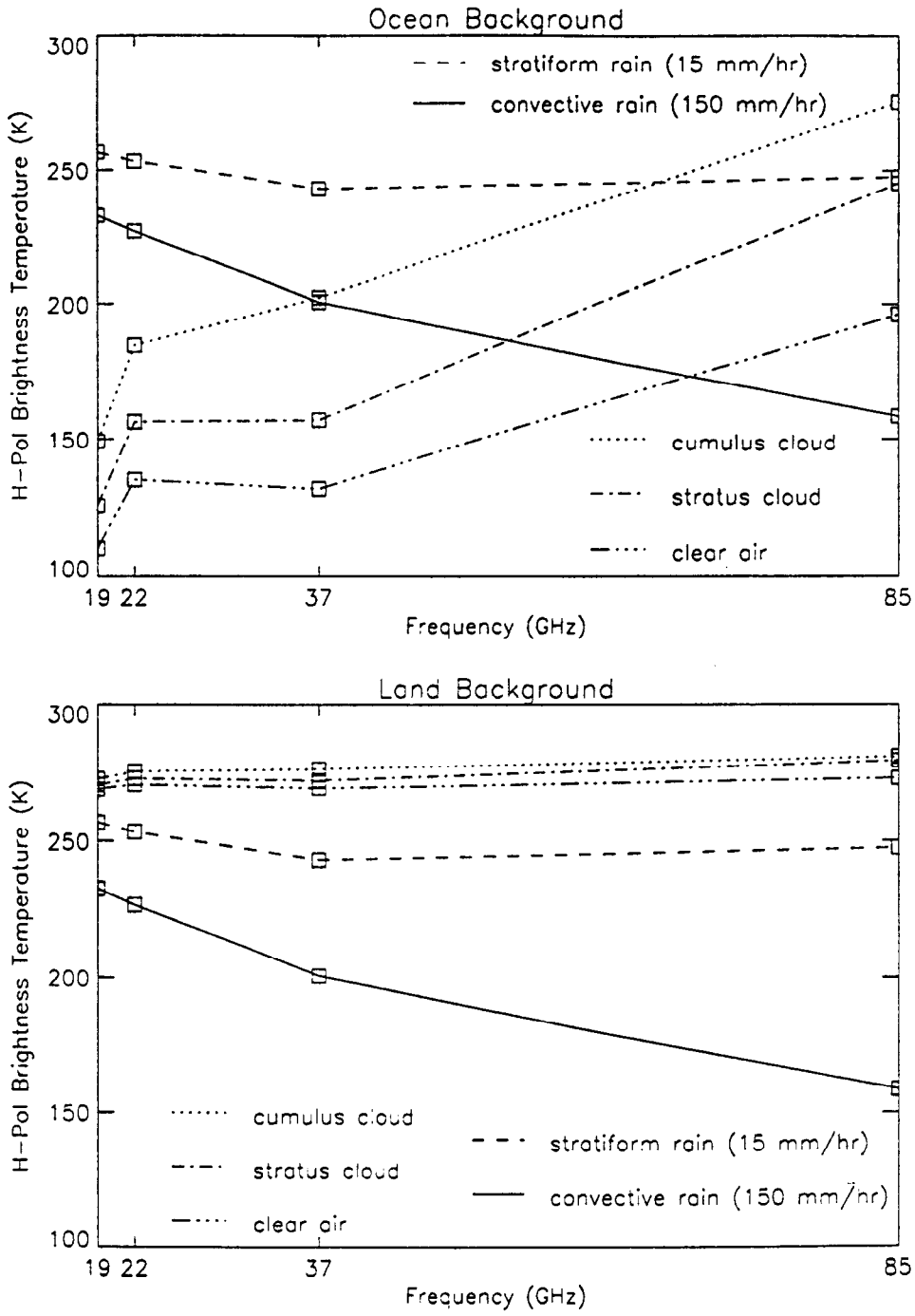

Figure 1.1: Model-generated brightness temperatures (horizontal polarization) versus frequency for five atmospheric conditions over calm ocean (top), and land with frequency-independent emissivity (bottom). (From [Burns *et al.*, 1993])

ple average but a weighted mean (reflecting the antenna pattern) dependent upon the spatial distribution of brightness temperatures (scene components) within the pixel. Further complicating factors are that the rain rate – brightness temperature relationship is generally nonlinear and that most algorithms use multiple channels, each with a different FOV.

The low repetition frequency with which PMI sensors sample a given point on the earth's surface is also a source of error. For mid-latitude regions this sampling rate is approximately twice per day; for low latitudes (tropics) it can be once every 2 days. Because of the short time scale of variation in the measured quantities, in situ and satellite measurements must be closely coincident in order to evaluate single retrievals. Clearly agreement will be improved by time averaging, but the exact time-space sampling pattern will determine how well estimates can produce a usable climatology for a given quantity [Kedem *et al.*, 1990].

Several studies of the sampling errors in rainfall estimates derived with satellite sensors have been carried out in the past few years [Shin and North, 1988; Bell *et al.*, 1990]. The emphasis has been on the TRMM satellite, but these studies indicate that the possible error to be even greater for the sun-synchronous orbiters such as those carrying the SSM/I and MIMR instruments. The effect of spatial averaging by satellite sensors was not accounted for in the sampling simulations in these studies. But this averaging effectively modifies the spatial statistics of the rainfield as observed by a sensor. Here we investigate the temporal and spatial sampling as well as spatial averaging characteristics simultaneously. Both SSM/I and MIMR sampling characteristics as well as those of Meteosat and AVHRR are considered. Evaluation of the sampling errors for the various satellite sensors is carried out on the meteorological radar rainfall observations from the AIP-2 data set. The beam-filling error resulting from the spatial averaging effect is examined in more detail and corrections are applied to a number of retrieval algorithms.

Data Sets

Two data sets are used in this investigation: the first is a data set of model-generated brightness temperatures, and the second consists of SSM/I data with coincident Meteosat and meteorological radar observations.

Model-generated brightness temperatures

The brightness temperature data were generated with a radiative transfer model developed by Kummerow and Liberti specifically for precipitating clouds (see also [Kummerow and Giglio, 1994] for a description of the model). Model radiances are calculated for a multilayered plane parallel atmosphere using Eddington's second approximation to the equation of radiative transfer. The vertical structure of the layered medium (cloud) must be specified in terms of the average relative humidity, cloud liquid water content, and precipitation rate of liquid and frozen hydrometeors in each layer. The height and temperature at each layer interface as well as the surface emissivity also must be specified.

The model includes the effects of both single and multiple scattering from precipitating hydrometeors with the Mie calculation of the extinction coefficients being carried out assuming the Marshall-Palmer drop size distribution for the liquid phase and in this study that from Sekon and Srivaastava [1971] for the solid phase. Drops of cloud liquid water are assumed to be too small to produce scattering at microwave frequencies so that only Rayleigh absorption is accounted for. Absorption coefficients for water vapor and atmospheric oxygen are also included in all levels; these are the sole contributors in levels not having cloud as well as in the clear sky case.

Model calculations produce top-of-atmosphere brightness temperatures for the geometry and frequency/polarization channels of the SSM/I instrument. In view of MIMR frequencies of 6.6 and 10.7 GHz are also included. Accuracies of 2-3 K in brightness temperature (not including errors due to finite cloud effects) are expected with this model.

Five atmospheric situations have been considered: clear air, stratiform nonprecipitating and precipitating clouds, and convective nonprecipitating and precipitating clouds. Information on the heights of the cloud bottom, the cloud top, and the boundaries of intermediate layers, as well as the total water content in each layer, was taken from Table 5-7 "Properties of Standard Cloud Models" in [Colwell, 1983].

The total water content must be partitioned between cloud droplets and precipitating hydrometeors. The drop size distribution of the hydrometeors in each layer (also given in the table) is described in terms of the mode radius and shape parameters of the modified gamma distribution from Deirmendjan [1964]. Assuming an upper cut-off of 100 μm for cloud droplets, this distribution is integrated over the small and large drop regimes to obtain cloud water content (CWC) and precipitating water content (PWC), respectively. The PWC is further partitioned between liquid (RWC) and frozen hydrometeors (IWC) depending on the temperature structure $T(z)$ in the cloud:

$T > 0°$ C	RWC= PWC	IWC= 0
-35° C $< T <$ 0° C	RWC= PWC $\cdot \frac{z(-35°\text{ C}) - z}{z(-35°\text{ C}) - z(0°\text{ C})}$	IWC= PWC − RWC
$T <$ -35° C	RWC= 0	IWC= PWC

As seen from Figure 1.2 the resulting CWC, RWC, and IWC profiles show distinctly different structures for convective and stratiform cases, the latter having very low RWC above the surface rain layer.

The model requires inputs of rain rate (RR) and of the precipitation rate for ice particles (IR). These are obtained from the relationship between RWC (or IWC) and the drop size distribution which is parameterized in terms of RR (or IR).

An internally consistent parameterization of relative humidity and temperature is obtained by specifying temperature and specific humidity profiles. The profiles used for the model calculations are illustrated in Figure 1.3. For layers without cloud and below the tropopause (starting at 10 km), the temperature profile decreases linearly from a surface value of T_0 with a constant lapse rate of Γ =-6.56 K/km. Inside the

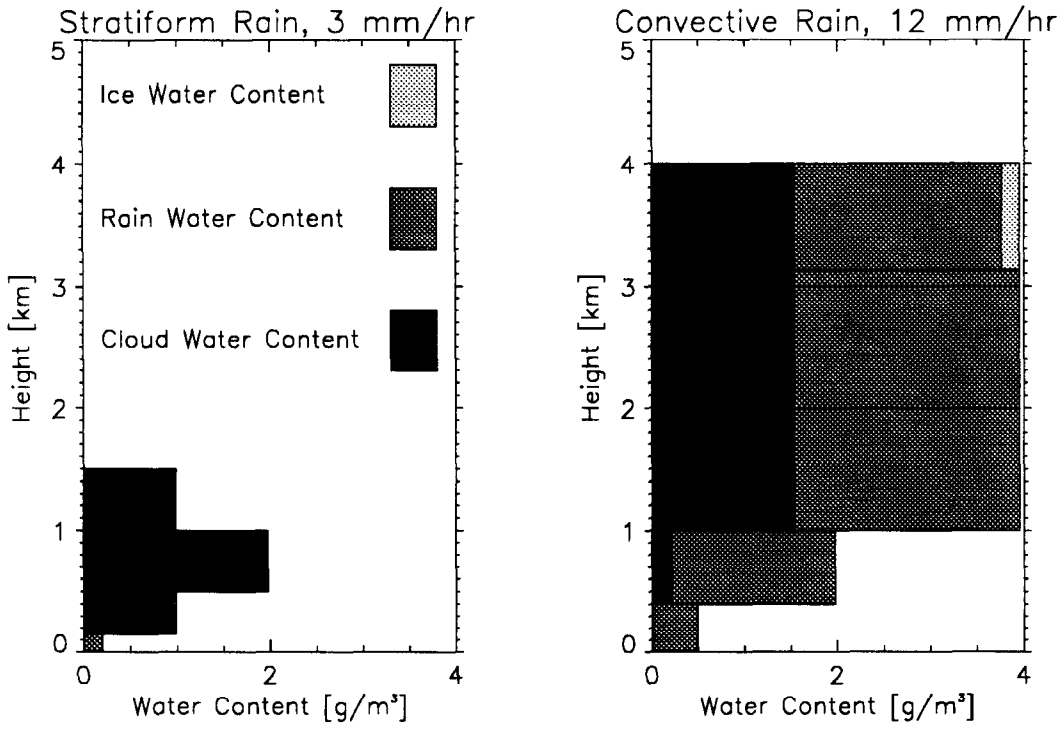

Figure 1.2: Water contents of stratiform and convective rain cloud.

cloud the profile follows a saturated adiabatic lapse rate, and assumes a constant temperature in the tropopause between 10 and 15 km. The specific humidity is assumed to decrease exponentially ($q = q_0 \exp(-z/\alpha)$) with height z. The surface value is calculated from the surface relative humidity (25%, 50%, 75%), and for α a value of 2 km was used (see Figure 1.3). The relative humidity outside the cloud was calculated from specific humidity and temperature according to [Rogers and Yau, 1991], using the same pressure profile as in the radiative transfer program. Inside the cloud the relative humidity was set to 100%.

The land surface types considered include wet soil, rocky soil, short grass, bare soil, and a mixture of bare and vegetated soils. The emissivities were taken from [Mätzler, 1990] and are given in Table 1.1. The surface temperature assumed was 290 K except for the surface temperature variation where it was varied from 280 K to 290 K.

Satellite and ground-based data

This data set is that used in the 2nd Algorithm Intercomparison Project (AIP-2) and was received from the U.K. Met Office (courtesy R. Allam). It is summarized in Table 1.2. It includes SSM/I and Meteosat image data as well as radar data from the FRONTIERS (Forecasting Rain Optimized using New Techniques of Interactively Enhanced Radar and Satellite) system [Browning, 1979] collected by the U.K. Met Office, and COST radar data from the European Radar Network developed under the

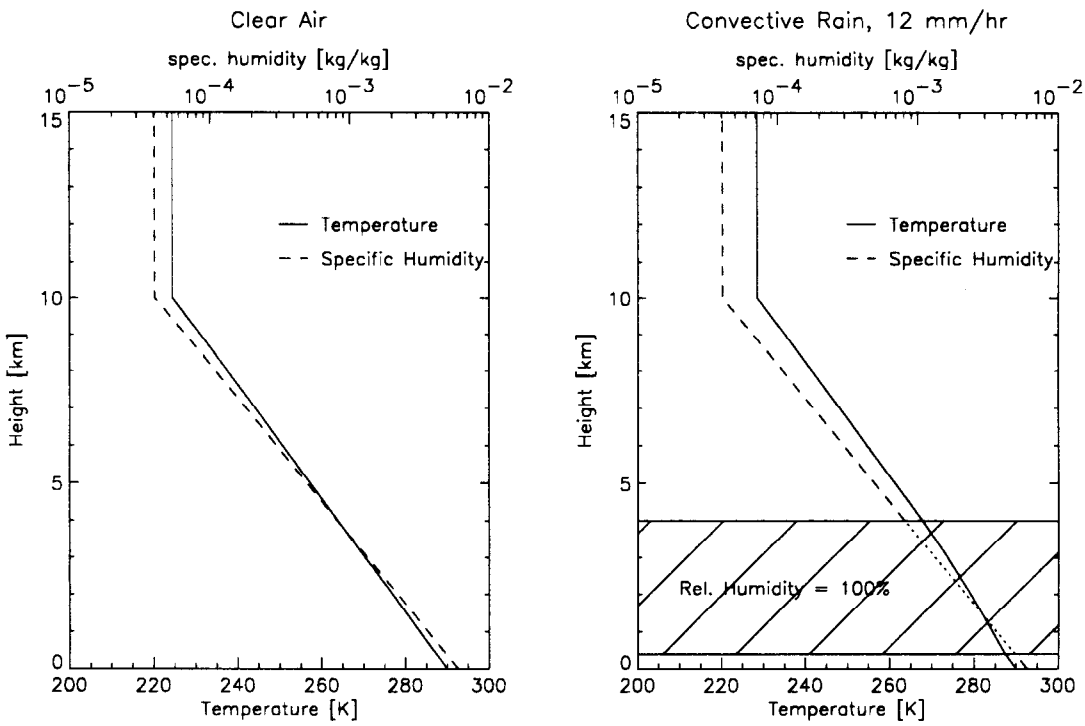

Figure 1.3: Model profiles for clear air (left) and convective rain cloud (right).

Table 1.1: Land Surface Emissivities

Channel	Wet Soil	Rocky Soil	Short Grass	Bare Soil	Mixed Surface
6.6 H	0.73	0.80	0.93	0.75	0.84
6.6 V	0.87	0.90	0.95	0.89	0.92
10.7 H	0.81	0.86	0.95	0.84	0.90
10.7 V	0.89	0.92	0.96	0.90	0.93
19 H	0.87	0.89	0.94	0.90	0.92
19 V	0.90	0.93	0.94	0.92	0.93
22 H	0.87	0.89	0.94	0.90	0.92
22 V	0.90	0.93	0.94	0.92	0.93
37 H	0.90	0.91	0.95	0.91	0.93
37 V	0.91	0.94	0.94	0.92	0.93
85 H	0.93	0.91	0.94	0.93	0.94
85 V	0.94	0.94	0.95	0.94	0.95

COST project [Collier, 1992]. The two sets of radar data differ in that the British FRONTIERS system data contain quality controlled instantaneous rain rates at 15 min intervals over the British Isles, whereas data from the European COST-73

system consist of instantaneous hourly data covering all of western Europe. Both datasets were supplied as pixel values in the AIP-2 Grid, with a spatial resolution of approximately 2.5 km. Hourly infrared data from the METEOSAT satellite (also in the AIP-2 grid) were supplied but not used in our analysis beyond selection of scenes. The SSM/I data were in Wentz Tape format (one tape for each sensor) that had to be divided into single scenes and projected to the AIP-2 grid for comparison with the radar data. Coordinate transformation was done only after brightness temperature specific analyses (for example, deconvolution, rain rate retrieval) had been carried out.

Table 1.2: AIP-2 data set

	Period	# of Scenes	Time Interval	Grid	Format
FRONTIERS Radar	01.02. - 09.04.91	5613	15 min	2.5 km	AIP-2 (720 × 600 pixels)
COST-73 Radar	01.02. - 31.03.91	1556	1 hr	2.5 km	AIP-2 (720 × 600 pixels)
METEOSAT IR	01.02. - 09.04.91	1498	1 hr	5 km	AIP-2 (360 × 300 pixels)
SSM/I F8	01.02. - 08.04.91	195	~ 12 hr (~ 1:45 hr)	25 km 12.5 km (85 GHz)	Wentz Tape
SSM/I F10	12.02. - 26.03.91	78	~ 12 hr (~ 1:45 hr)	25 km 12.5 km (85 GHz)	Wentz Tape

Description of Algorithms

Most algorithms for rain retrieval over land rely on the scattering signature of rain for its detection and measurement. As seen in Figure 1.1, the presence of rain clouds over land primarily leads to a decrease of the Tb compared with a cloud free atmosphere which is greatest at the highest frequencies (e.g 85 GHz). This results from scattering of microwave radiation by rain drops and ice particles. Because scattering is not unique to rain and ice clouds, so called "screening" algorithms have to be applied before rain rate can be calculated. The purpose is to separate rain clouds from other surfaces such as desert and snow-covered terrain, which can also result in low values of Tb at 85 GHz. These algorithms are independent of the rain rate algorithms and therefore are treated separately.

Screening algorithms

Before calculating the rain rate, rain areas first have to be detected. The methods used for this detection of "screening" can be divided into three categories:

1. Small polarization difference ($Tb_V - Tb_H < Tb_{Threshold}$) is used successfully over ocean for rain detection. This method depends on the attenuation of the polarized surface signal by the overlying cloud, and is therefore not satisfactory

over land because the signal emitted by the surface is not necessarily polarized. Also small polarization differences need not be caused by clouds alone.

2. Absolute Tb can indicate the presence of precipitation. Lower frequency Tb are less reduced by scattering in the cloud than those of the higher frequency channels. However, determining absolute Tb thresholds does not always account for surface temperature influences, so regional and seasonal temperature variations may lead to misclassification.

3. Tb scatterplots using two or more channels can be used in a classification process. Land, ocean or precipitation pixels can be identified from their positions in the plot.

A screening test often used is that of Grody [1991] which is a combination of methods 2 and 3. Grody defines a Scattering Index (SI) by fitting the no-rain antenna temperatures (Ta) of the other channels against the 85 GHz Ta:

$$\mathrm{Ta}_{85\mathrm{V}} = a - b \cdot \mathrm{Ta}_{19\mathrm{V}} - c \cdot \mathrm{Ta}_{22\mathrm{V}} - d \cdot \mathrm{Ta}_{22\mathrm{V}}^2 \qquad \text{(fitting with no rain cases)} \quad (1.1)$$

$$SI = a - b \cdot \mathrm{Ta}_{19\mathrm{V}} - c \cdot \mathrm{Ta}_{22\mathrm{V}} - d \cdot \mathrm{Ta}_{22\mathrm{V}}^2 - \mathrm{Ta}_{85\mathrm{V}} \quad (1.2)$$

If SI is below a certain threshold, i.e. scattering effects are too small, then there is no surface scattering and no cloud. If Tb_{22V} is below a threshold temperature and, at the same time, too cold compared with Tb_{85}, a snow or ice surface is indicated. In case of a cloud-free situation over a desert sand surface, Tb_{19} is expected to exceed a certain value. If none of the tests is true, precipitation is detected.

Smith *et al.* [1992] modifies the Grody screening algorithm by suggesting latitude dependent tests. So the desert test is done only between 30° N and 30° S. They also give latitude-dependent upper limits on SI for detection of precipitation. In addition they calculate the "Polarization Corrected Temperature (PCT)" [Spencer *et al.*, 1989] for Tb_{85}

$$PCT = (1 + t) \cdot \mathrm{Tb}_{85\mathrm{V}} - t \cdot \mathrm{Tb}_{85\mathrm{H}} \quad (1.3)$$

where t is an empirically determined constant. If the PCT is too large, i.e. the Tb_{85} too warm, there is no precipitation.

Method 3 is used by Adler *et al.* [1993] who identify precipitation with a Tb_{37} vs Tb_{85} scatterplot (method 3). Certain areas in this diagram are identified as land surfaces (high Tb_{37} and high Tb_{85}), ocean (low Tb_{37}, Tb_{85} low but considerably higher than Tb_{37}) and precipitation (Tb_{37} increased, Tb_{85} decreased compared with no rain situations).

The determination of a rain/no-rain threshold and the land/ocean test are implicitly done in the rain rate algorithms of Barrett, Barrett and Kidd and Barrett and Todd [Allam *et al.*, 1993] when determining the algorithm coefficients. Only the Grody snow/ice surface screening test is applied. Likewise the inversion techniques of Kummerow and Giglio [1994] and Marzano *et al.* [Basili *et al.*, 1993] do not require an additional screening algorithm. By including model situations for various land and water surfaces without precipitation in their comparison data sets, screening is done implicitly.

Rain rate algorithms

The description of rain rate algorithms given here are based primarily on documentation from the AIP-2 and PIP-1 algorithm intercomparison projects [Allam *et al.*, 1993; Kniveton *et al.*, 1994] with supplemental information in cases where the algorithm has been published in the open literature. Only those algorithms used in our further investigations, i.e. those easily implemented and for which coefficients are available, are described. For more information the reader is referred to the documentation cited or the review article of Liberti [1994].

As mentioned earlier the strongest signal for rain is in the Tb_{85}, and therefore all algorithms use the Tb_{85} for rain rate retrieval over land. An algorithm that uses the 85 GHz channel alone for rain rate calculation is that from Adler *et al.* [1993] (**adler** algorithm).

$$RR = 59.9 - 0.239 \cdot \mathrm{Tb}_{85\mathrm{H}}. \tag{1.4}$$

The Tb_{37} are needed only to select precipitation areas (see Screening above). After finding the areas with precipitation the coefficients for the RR-Tb relationship are derived from high resolution model calculations averaged over a SSM/I footprint. Thus the beam-filling effect is simulated. The process was developed using data from the first Algorithm Intercomparison Project (AIP-1) over Japan. Hence the input for the model calculations are clouds typical for conditions around Japan. The influence this has on the quality of the algorithm results for different geographical regions remains to be investigated.

The influence of surface temperature and emissivity on Tb_{85} can be compensated for by including the other SSM/I frequencies in the calculations. Hence Barrett [Allam *et al.*, 1993] uses an "Adjusted Frequency Difference (AFD)"

$$AFD = a \cdot \mathrm{Tb}_{37\mathrm{V}} - \mathrm{Tb}_{85\mathrm{V}} - b \tag{1.5}$$

for rain rate calculations (**barrett** algorithm)

$$RR = c \cdot AFD + d \cdot AFD^2. \tag{1.6}$$

Here Tb_{37} is effectively modified so that it equals Tb_{85} for no rain cases (i.e. $AFD = 0$). An AFD different from zero is then caused by precipitation. The coefficients a and b are determined from a $\frac{\mathrm{Tb}_{85\mathrm{V}}}{\mathrm{Tb}_{37\mathrm{V}}}$ histogram. The histogram is either made for each SSM/I scene and therefore varies temporally or it is calculated for each pixel from a time series of different scenes and then varies spatially. The rain rate coefficients c and d come from a non-linear regression of Tb against FRONTIERS radar data over the British Isles. However neither numeric coeffficients are available for this algorithm nor are the differrent means for the determination of the coefficients at our disposal.

The algorithm of Grody and Ferraro makes use of the influence of scattering by clouds on Tb_{85} as estimated by the Scattering Index (SI) [Grody, 1991] (see Screening above). Rain rate is assumed to depend linearly on SI, and two relationships are suggested, one valid globally

$$SI_G = [256.17 - 0.375 \cdot \mathrm{Ta}_{19\mathrm{V}} - 0.200 \cdot \mathrm{Ta}_{22\mathrm{V}} + 0.0237 \cdot \mathrm{Ta}_{22\mathrm{V}}^2] - \mathrm{Ta}_{85} \tag{1.7}$$

$$RR = -1.65 + 0.289 \cdot SI_G, \tag{1.8}$$

and one valid over land only (**ferraro** algorithm)

$$SI_L = [438.5 - 0.46 \cdot \mathrm{Ta_{19V}} - 1.735 \cdot \mathrm{Ta_{22V}} + 0.00589 \cdot \mathrm{Ta_{22V}^2}] - \mathrm{Ta_{85V}} \tag{1.9}$$

$$RR = -2.71 + 0.362 \cdot SI_L. \tag{1.10}$$

The coefficients are derived from regressions of SSM/I data against AMeDAS radar data over Japan and FRONTIERS data over Great Britain. By compositing these data sets the effect of regional variations on derived rain rates is supposedly reduced.

Ferriday [Allam *et al.*, 1993] suggests an algorithm that uses all four vertical polarization channels of the SSM/I. Choosing vertical polarization reduces influences of different surface wetnesses. Equal numbers of channel additions and subtractions reduce the bias introduced by surface temperature or emissivity variations. The lower frequency Tbs are increased by precipitation because of emission effects, the two higher frequency Tb are reduced by rain clouds because of scattering. This leads to the **ferriday** RR-Tb relationship

$$RR = \frac{1}{a} \cdot (\mathrm{Tb_{19V}} + \mathrm{Tb_{22V}} - \mathrm{Tb_{37V}} - \mathrm{Tb_{85V}}) + b. \tag{1.11}$$

Calculations with model clouds using the Kummerow radiative transfer program showed the best algorithm results for $a = 7$ and $b = 0$.

Before the launch of the first SSM/I a D-Matrix rain rate algorithm had been developed by the sensor manufacturer. During the first year of operation this algorithm was tested against radar data from tropical latitudes [Olson *et al.*, 1991]. It was found that a linear relationship between rain rate and Tb did not give satisfactory results. Hence an exponential relationship (**calval** algorithm) was chosen:

$$RR = \exp\left(a_0 + \sum_{i=1}^{7} a_i \cdot Tb_i\right) - c \tag{1.12}$$

Regression of tropical radar data against SSM/I Tb-data led to the following two algorithms for over land use, the second being valid when the 85 GHz channel is not available:

$$RR = \exp(3.29716 - 0.01290 \cdot \mathrm{Tb_{85V}} + 0.00877 \cdot \mathrm{Tb_{85H}}) - 8 \tag{1.13}$$

$$RR = \exp(-17.76849 - 0.09612 \cdot \mathrm{Tb_{37V}} + 0.15678 \cdot \mathrm{Tb_{19V}}) - 1 \tag{1.14}$$

The coefficient c depends on latitude and longitude. It remains to be seen whether the coefficients for tropical areas (shown here) give optimal results in mid-latitudes.

Smith *et al.* [1992] derived a simple algorithm from their results of brightness temperature calculations based on a numerical model for rain cloud development. They tested the relationship

$$RR = a_0 + a_1 \cdot \mathrm{Tb_{19}} + a_2 \cdot [\mathrm{Tb_{19}} - \mathrm{Tb_{22}}] + a_3 \cdot [\mathrm{Tb_{19}} - \mathrm{Tb_{37}}] + a_4 \cdot [\mathrm{Tb_{19}} - \mathrm{Tb_{85}}] \tag{1.15}$$

(**smith** algorithm) and found that Tb_{19} explained 83 % of the variance found in the model data. Based on the statistical significance of each channel, the optimal algorithm for the model data was

$$RR = 125.5 - 0.455Tb_{19} + 0.108 \cdot (Tb_{19} - Tb_{85}) \tag{1.16}$$

$$Tb_i = (\mathrm{Tb_{iH}} + \mathrm{Tb_{iV}})/2. \tag{1.17}$$

Comparison of rain rates derived with this relationship with the model data the coefficients were derived from showed large scatter (deviations up to 18 mm/hr) especially at high rain rates. Smith *et al.* [1992] therefore suggest that a multichannel profiling algorithm should be used to derive distinct features of the hydrometeor profile, and the calculation of the rain rate done as a second step.

Sensitivity to Surface Variations

Five of the algorithms (**ferraro**, **ferriday**, **calval**, **adler** and **smith**) were chosen to look at the effect of changes in atmospheric and surface conditions on retrieved rain rate. These algorithms were applied to the model-generated brightness temperatures described above. The results of the **calval** algorithm are not shown because the retrieved rain rates were nearly zero for all raining clouds.

Most algorithms produced reasonable rain rates in a relative sense only (i.e. comparing different cloud models) although the absolute values were not necessarily comparable with the model rain rates or between algorithms. This is primarily due to the determination of algorithm coefficients with regressions against data or model results of which the models used here are not representative. The rain rate values were also often very small or negative, which meant that no screening schemes could be evaluated. Also most screening algorithms use the signature of an increasing depression at 85 GHz and an increasing 19 GHz Tb with increasing rain rate, which is not present in our model-generated data. Therefore we restricted our investigation to looking at only the changes in rain rates retrieved. Any effect of a bias between algorithm results and model rain rates was thus eliminated.

The changes in retrieved rain rates were calculated from the Tb dataset described above assuming first that rain clouds fill the radiometer beam completely and then only partially, with either non-raining clouds or clear air as the other component.

Surface type sensitivity

The effect of surface type variability on brightness temperatures is shown in Figure 1.9. This depicts the change in the Tb induced by a change in surface emissivity from that of wet soil to that of short grass for identical atmospheres. The frequency dependence reflects that of the emissivities (see Table 1.1). At 22 GHz and below, the variability in Tb produced by changes in surface emissivity is greater than that due to changing cloud properties (i.e. water content). This leads to ambiguities between clear, cloudy, and raining conditions at these frequencies. At 37 and 85 GHz surface emissivity variations have little if any effect on the modelled brightness temperatures of rain clouds. If the cloud is optically thick the satellite cannot measure

the change in surface emissivity as all radiation emitted by the surface is absorbed by the cloud and the radiation reaching the sensor is that emitted by the cloud. This saturation is reached earlier (i.e. for clouds with less water) for higher frequencies than for lower frequencies.

Rain rate changes caused by the variation of surface type and surface temperature are shown in Figure 1.9 (right). Surface type variations caused the lowest Tb changes at 85 GHz so that the small change in the **adler** RR could be expected. The 19 and 22 GHz Tb showed the largest effect with changing the surface type. Thus the large ΔRR for **ferraro** (which depends heavily on the 22 GHz channel) can be explained. The **smith** algorithm uses 19 and 85 GHz Tb with the same sign to calculate rain rates. As both these Tb are changed in the same direction, the resultant RR change is the largest of all algorithms. The ΔRR for **ferriday** are smaller than for **ferraro** but not negligible, indicating that the algorithm cannot compensate for surface type variations though this was explicitly considered in its design, because the Tb variations for different channels are not of the same size. Thus using differences between Tb to calculate the rain rate is not enough to cancel out surface type effects.

Surface temperature sensitivity

Brightness temperature variations caused by a change of the surface temperature from 280 K to 290 K are shown in Figure 1.10 (left). A surface temperature change of 10 K results in a change in the temperature of the whole atmosphere by the same amount. Note that surface relative humidity is not changed so that an increase in surface temperature causes an increase in water vapor content in all but the cloud layers. For thin clouds the Tb variations are of the same size as the temperature variation (10 K). The effect on the water vapor content can be observed in the slightly larger change of the Tb for 22 GHz than for 19 GHz. Varying the temperature of cloud layers changes the partitioning between ice and liquid water content. An increase in layer temperature results in an increase of liquid and a decrease of ice water content. For the 85 GHz channel this leads to a decrease in scattering so that the Tb is increased even further than by the amount of the actual temperature change. For the lower frequencies more water and less ice means more scattering, thus those Tbs are increased by an amount smaller than the layer temperature increase. Both effects can be seen in the case of the convective 2 mm/hr rain cloud.

Figure 1.10 (right) shows the RR changes caused by the 10 K change in surface temperature. Since the Tb were increased for all clouds and all channels, all algorithms show a reduction of the retrieved rain rate. Algorithms that do not use a difference between the Tb of different channels (**adler** and **smith**) show the largest RR variations, whereas the **ferriday** algorithm can compensate for surface temperature effects very well. The **ferraro** algorithm shows comparatatively large RR variations for the convective cases. This might be caused by the different behavior of the 85 GHz and the other Tb. The assumption behind **ferraro** (85 GHz Tb can be approximated by a linear combination of lower frequency Tbs) causes the algorithm to calculate larger RR when the difference between 85 GHz and the other Tb is

increased. For stratiform cases, where the Tb variations are almost the same for all channels, **ferraro** shows much smaller ΔRR.

The sensitivity of these algorithms to atmospheric variations has been presented in the paper by Burns and Flender [1994]. It was found that Tb variations caused by changes in surface relative humidity from 50% to 25% and 75% and total cloud liquid water variation of $\pm 30\%$ were larger for the lower frequency (19, 22 GHz) than for the higher frequency (85 GHz) channels. Algorithms making use only of high frequency Tb (**adler**) therefore showed the smallest variations in retrieved rain rate ($\leq$ 0.5 mm/hr) due to atmospheric variations. Algorithms including low frequency Tb were especially sensitive to cloud liquid water variations, showing errors in retrieved rain rate of up to 2 mm/hr. Sensitivity to variations in relative humdity was found to be very low ($\leq$ 0.3 mm/hr) even in partial beam-filling situations. Comparing these results to those presented above shows that the surface variations have a much larger effect on both brightness temperatures and rain retrieval results of most algorithms than do variations in the investigated atmospheric parameters.

Application to SSM/I Data

The availability of the AIP-2 data set allows evaluation of the rain rate algorithms in a statistically significant manner not possible with the limited brightness temperature data set generated with the radiaitve transfer model. As meteorological radar data are included in the AIP-2 data set, the evaluation presented here concentrates on comparing actual rain rate retrievals, using the radar data as truth.

Figures 1.4 and 1.5 show scatterplots of rain rates retrieved from SSM/I data with both original and recalibrated (see below) algorithms vs. radar rain rates for the scene shown in Figure 1.11. Retrievals using the original coefficients show large biases for all algorithms except the **calval**, but the rain rates retrieved with this algorithm almost do not correlate with the radar rain rates. Because of these large biases the difference between bias and rms values is small, most of the error being due to the bias. These results are representative of those presented in the AIP-2 pre-workshop [Allam *et al.*, 1993] and the workshop [WMO, 1994] reports.

As already suggested in the case of applying algorithms to model-generated data in this study, one possible source of the large discrepancy between algorithm results and ground truth is that the algorithms have been calibrated (i.e. algorithm coefficients determined) using data not representative of rain systems in the British Isles and western Europe area. In order to compare the rain rate algorithm concepts we re-calibrated the rain rate algorithms using the AIP-2 data set.

Algorithm recalibration

SSM/I-pixels were projected into the AIP-2 grid. Only pixels with measurements at all four SSM/I frequency channels (19, 22, 37 and 85 GHz) were used. If a pixel was more than 30 km (12 AIP-2 pixels) inshore and if radar derived rain rates were available in the temporally nearest FRONTIERS scene, an average of rain rates within a radius of 12.5 km (5 AIP-2 pixels) of the SSM/I pixel was taken as the ground truth value (see Figure 1.11b). The temporal interval between two FRONTIERS scenes

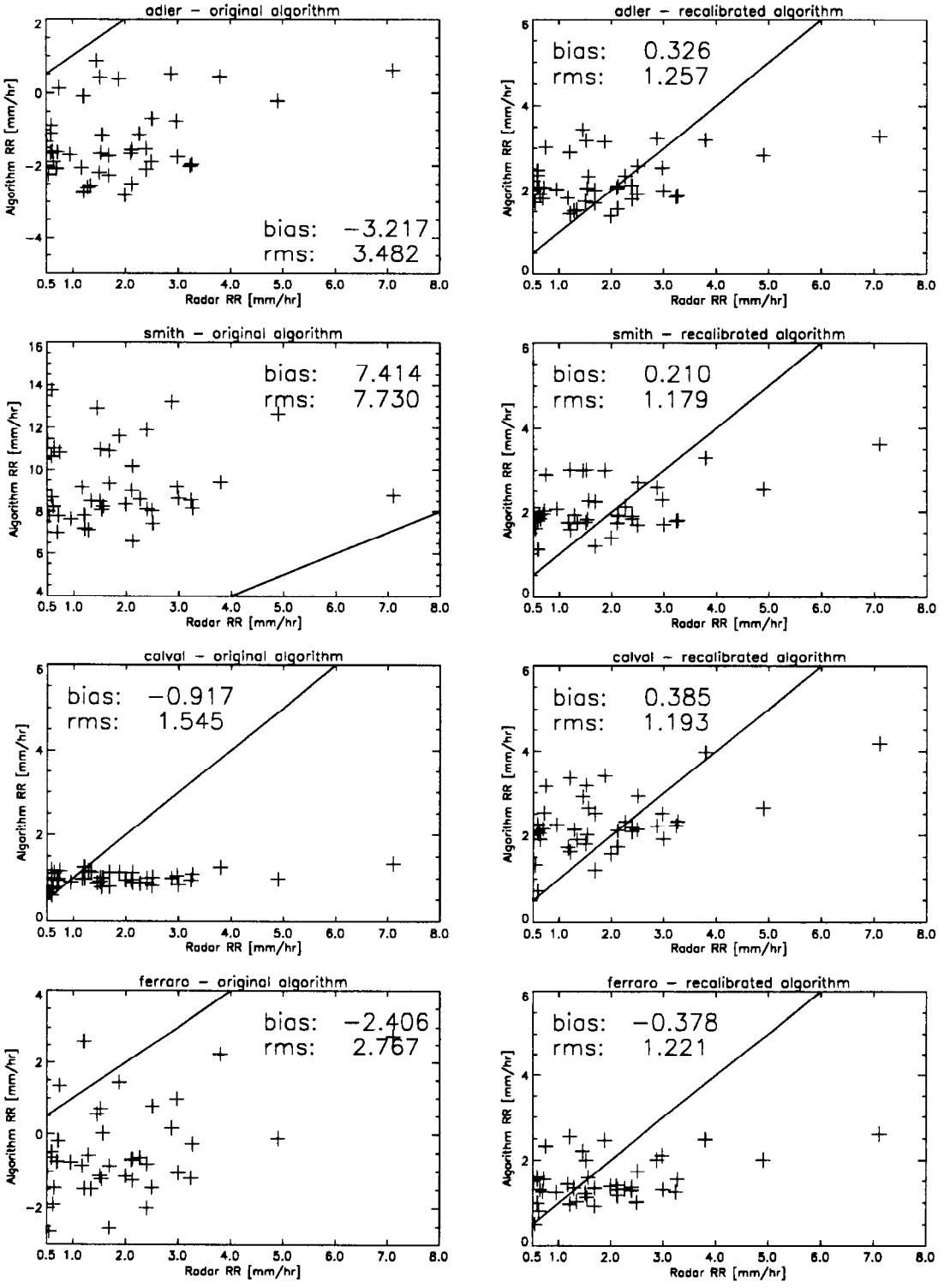

Figure 1.4: Scatterplots of retrieved rain rates vs radar rain rate for SSM/I scene 910302.1850.

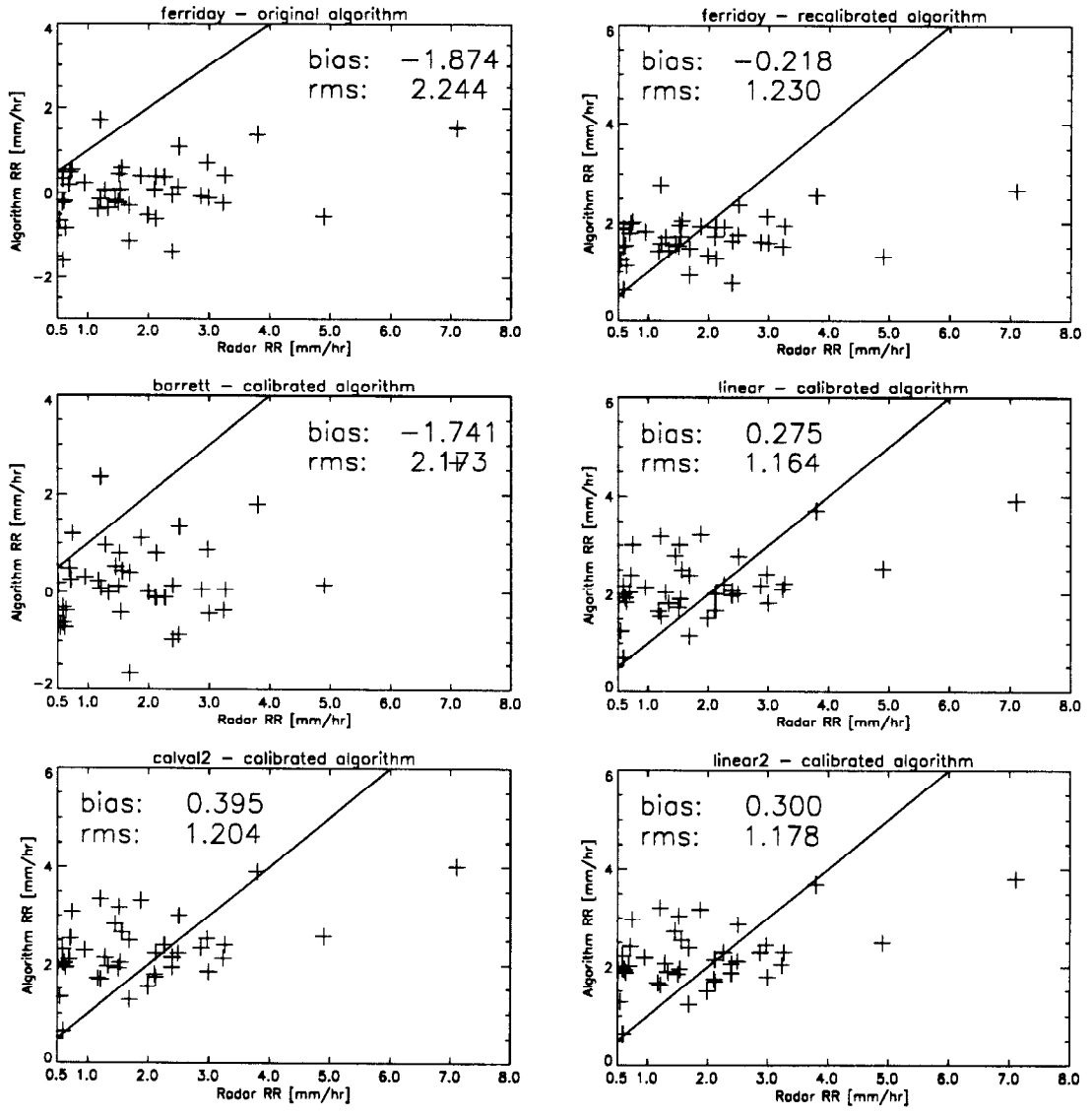

Figure 1.5: Scatterplots of retrieved rain rates vs radar rain rate for SSM/I scene 910302.1850.

was 15 minutes, so the maximum temporal displacement is about 8 min. The worst spatial collocation error is one AIP-2 pixel ($\approx$ 2.5 km). Vectors consisting of seven SSM/I brightness temperatures and an averaged radar rain rate were divided into raining and non-raining cases using a threshold of 0.5 mm/hr. In total there were 5589 vectors, 489 of them with rain (>0.5 mm/hr).

The coefficients of each rain rate algorithm were determined by multilinear regression of the brightness tempreatures or brightness temperature combinations, as specified in the original algorithm, against the average radar rain rate. Thus the value of

$$\chi^2 = \frac{1}{N}\sum_{i=1}^{N}\left(\frac{RR_{\text{radar}} - RR_{\text{algorithm}}}{\Delta RR_{\text{radar}}}\right)^2 \tag{1.18}$$

was minimized where RR_{radar} is the average radar RR, $RR_{\text{algorithm}}$ the retrieved RR, and ΔRR_{radar} the uncertainty of the radar rain rate. All average RR were expected to have the same uncertainty, so the actual value of ΔRR_{radar} does not influence the quality of the fit. If ΔRR_{radar} is chosen as 1 mm/hr (which is certainly a large overestimate), the minimized χ^2 is equal to the squared rms error of the re-calibrated algorithm.

The set of vectors was divided randomly into a training set and a test set. Only the rain vectors in the training set were considered for the fits, except where some of the algorithm coefficients were determined from no-rain cases (Scattering Index, Adjusted Frequency Difference). In this cases the non-raining cases of the training set were used for algorithm calibration, too.

The values of the coefficients for the original and the recalibrated algorithms are shown in Table 1.3. Table 1.4 shows the rms error and the correlation between retrieved and radar rain rates for the "old" and "new" algorithms. No entry under "old" for **barrett** is shown because no algorithm coefficients were given in the AIP-2 documentation.

In addition to the algorithms described above a linear Tb-RR relationship considering all frequencies (**linear** $RR = \sum a_i \cdot Tb_i$) was also fitted.

The effect of the recalibration is to reduce the rms error even for the test set data by a factor of between 0.75 and 0.21. The rms error for the training set data is, of course, even lower. The very large decrease in the rms error for the **adler** and **smith** algorithm is due to the large bias ($\approx$ 4 mm/hr for **adler** and $\approx$ 5 mm/hr for **smith**) with the original algorithms.

The correlation only barely changed with the recalibration of the **ferriday**, **ferraro** and the **adler** algorithms, but was significantly improved for **calval** and **smith**. Thus it is shown that without the recalibration a comparison of algorithm results would mainly compare the datasets the original algorithms were fitted to with the actual dataset but would not show how well the algorithm concepts could represent the actual Tb-RR relationship.

The worst performance is shown by the **barrett** algorithm. This is due to the fact that there is no offset coefficient used in the RR-AFD relationship. Though this coefficient is not necessary if the idea behind the algorithm ($AFD = 0$ for no-rain cases) is right, a small offset coefficient might have reduced the difference between retrieved and radar rainrates (especially $<$ 1mm/hr).

Both **barrett** and **ferraro** algorithms require a double fit of two relationships to two complementary data sets (rain and no-rain data). The ambiguities between these two data sets, which are a consequence of both the necessity to define a rain/no-rain threshold and the ambiguities in the Tb-RR relationship due to cloud liquid water variability, smear out the theoretical assumption of $SI = 0$ or $AFD = 0$ exactly for no-rain situations. This might explain the comparatively poor performance of the **ferraro** algorithm. Though it allows an offset coefficient for the SI-RR relationship it does not show better results than other "simpler" algorithms. Another reason might be the strong dependence of the **ferraro** algorithm on the 22 GHz Tb. The coefficient for this channel in the linear algorithm is rather small, indicating that the 22 GHz Tb are not very strongly correlated with the radar rain rate.

Table 1.3: Algorithm coefficients

adler: $RR = a_0 - a_1 \cdot \mathrm{Tb}_{85\mathrm{H}}$

	a_0	a_1
orig.	59.9	0.239
recal.	36.3	0.133

calval: $RR = \exp(a_0 + a_1 \cdot \mathrm{Tb}_{19\mathrm{H}} + a_2 \cdot \mathrm{Tb}_{19\mathrm{V}} + a_3 \cdot \mathrm{Tb}_{22\mathrm{V}} + a_4 \cdot \mathrm{Tb}_{37\mathrm{H}} + a_5 \cdot \mathrm{Tb}_{37\mathrm{V}} + a_6 \cdot \mathrm{Tb}_{85\mathrm{H}} + a_7 \cdot \mathrm{Tb}_{85\mathrm{V}}) - c$

	a_0	a_1	a_2	a_3	a_4	a_5	a_6	a_7	c
orig.	3.297	0.0	0.0	0.0	0.0	0.0	-0.0129	0.00877	8
recal.	5.469	0.0020	-0.00519	0.00170	0.00585	-0.00656	-0.00062	-0.00534	25

ferriday: $RR = a_0 + a_1 \cdot (\mathrm{Tb}_{19\mathrm{V}} + \mathrm{Tb}_{22\mathrm{V}} - \mathrm{Tb}_{37\mathrm{V}} - \mathrm{Tb}_{85\mathrm{V}})$

	a_0	a_1
orig.	0.0	0.143
recal.	1.66	0.092

linear: $RR = a_0 + a_1 \cdot \mathrm{Tb}_{19\mathrm{H}} + a_2 \cdot \mathrm{Tb}_{19\mathrm{V}} + a_3 \cdot \mathrm{Tb}_{22\mathrm{V}} + a_4 \cdot \mathrm{Tb}_{37\mathrm{H}} + a_5 \cdot \mathrm{Tb}_{37\mathrm{V}} + a_6 \cdot \mathrm{Tb}_{85\mathrm{H}} + a_7 \cdot \mathrm{Tb}_{85\mathrm{V}}$

	a_0	a_1	a_2	a_3	a_4	a_5	a_6	a_7
cal.	56.28	0.04626	-0.1238	0.04352	0.1423	-0.1557	-0.01400	-0.1424

smith: $RR = a_0 + a_1 \cdot \mathrm{Tb}_{19} + a_2 \cdot [\mathrm{Tb}_{19} - \mathrm{Tb}_{22}] + a_3 \cdot [\mathrm{Tb}_{19} - \mathrm{Tb}_{37}] + a_4 \cdot [\mathrm{Tb}_{19} - \mathrm{Tb}_{85}]$

	a_0	a_1	a_2	a_3	a_4
orig.	125.5	-0.455	0.0	0.0	0.108
cal.	38.2	-0.138	0.1163	-0.116	0.163

ferraro: $SI = a_0 + a_1 \cdot \mathrm{Tb}_{19\mathrm{V}} + a_2 \cdot \mathrm{Tb}_{22\mathrm{V}} + a_3 \cdot \mathrm{Tb}_{22\mathrm{V}}^2 - \mathrm{Tb}_{85\mathrm{V}}$

$RR = a_4 + a_5 \cdot SI$

	a_0	a_1	a_2	a_3	a_4	a_5
orig.	438.5	0.46	-1.735	0.00589	-2.71	0.362
cal.	1887	-1.303	-11.99	0.0271	1.24	0.133

barrett: $AFD = a_0 + a_1 \cdot \mathrm{Tb}_{37\mathrm{V}} - \mathrm{Tb}_{85\mathrm{V}}$

$RR = a_2 \cdot AFD + a_3 \cdot AFD^2$

	a_0	a_1	a_2	a_3
cal.	-55.26	1.218	0.2767	0.00051

Table 1.4: Algorithm performances

	recalibrated			original	
	$\text{rms}_{training}$	rms_{test}	corr.	rms	corr.
ferraro	1.377	1.439	0.450	2.378	0.461
ferriday	1.412	1.511	0.377	2.125	0.377
adler	1.325	1.368	0.519	4.041	0.519
smith	1.299	1.397	0.518	5.962	0.192
calval	1.281	1.342	0.559	1.806	0.414
linear	1.282	1.343	0.553		
barrett	1.728	1.934	0.389		

Comparing the two-coefficient algorithms **ferriday** and **adler** shows that using one 85 GHz channel describes the rain rate better than an equal weight combination of four channels. The quality of the results of these two and the other algorithms increases with the number of coefficients they use.

The results of the **smith** algorithm are better than those for the **adler** algorithm for the training set, which is expected since **smith** uses more parameters, but worse for the test set data. Probably the additional channels induce too much scatter which increases the rms error for data sets the algorithm is not calibrated for. The **smith** algorithm can be rewritten in the same way as the **linear** algorithm but using the average H and V-Pol temperatures for all but the 22 GHz channels:

$$RR = 38.2 + 0.025 \cdot \text{Tb}_{19} - 0.116 \cdot \text{Tb}_{22V} + 0.116 \cdot \text{Tb}_37 + -0.163 \cdot \text{Tb}_{85}. \quad (1.19)$$

The 19 GHz coefficient is the smallest, whereas the 85 GHz channel has the greatest effect on the retrieved rain rate.

The **linear** and **calval** algorithms show the best performances. Their rms and correlation values are almost equal. This can be explained by the large offset coefficient c for the recalibrated **calval** algorithm. The variation in the value of the exp(...) term ($\approx$ 8 mm/hr) is comparatively small compared with the absolute value (25–33 mm/hr), thus the exp-function can be easily linearly approximated. Both algorithms also show the best rms values for the test set. Here the additional scatter induced by the additional channels in total seems to be less than for the **smith** algorithm.

A major difference between the old and new coefficients for the calval algorithm is the fact that the low frequency coefficients are no longer zero, though some are small compared to the others. For these coefficients (a_1, a_3, a_6) the uncertainties (not shown) are of the same order as the absolute values of the coefficients. The same is true for the analogue coefficients (a_1, a_3, a_6) of the linear algorithm.

The performance of these algorithms calibrated to the training data set but with a_1, a_3 and a_6 set to zero is shown in Table 1.5. The differences in the rms and correlation values are still negligibly small. They both still outperform all other algorithms in both rms and correlation values, though, as could be expected, they do not work so well as their "full" versions.

Table 1.5: Modified algorithms

calval2: $RR = \exp(a_0 + a_1 \cdot \mathrm{Tb}_{37\mathrm{H}} + a_2 \cdot \mathrm{Tb}_{37\mathrm{V}} + a_3 \cdot \mathrm{Tb}_{85\mathrm{V}}) - c$

	a_0	a_1	a_2	a_3	c
recal.	5.207	0.005243	-0.006739	-0.005060	30

linear2: $RR = a_0 + a_1 \cdot \mathrm{Tb}_{37\mathrm{H}} + a_2 \cdot \mathrm{Tb}_{37\mathrm{V}} + a_3 \cdot \mathrm{Tb}_{85\mathrm{V}}$

	a_0	a_1	a_2	a_3
cal.	54.14	0.1511	-0.1903	-0.1576

	recalibrated		
	$\mathrm{rms}_{training}$	rms_{test}	corr.
calval2	1.284	1.360	0.548
linear2	1.286	1.360	0.543

Note that for both algorithms coefficients on the two 37 GHz channels are are not equal. This explains why the 22 GHz coefficient of the **smith** algorithm (using polarization-averaged Tb) was not small and the algortihm showed a slightly worse performance.

The effect of the recalibration for a single scene is shown in Figures 1.4 and 1.5. Bias values are now well below the rms values, except for the **barrett** algorithm, where the recalibration could not compensate for any bias because of the missing offset coefficient. The scatterplots for the recalibrated **adler**, **smith** and **calval** algorithms and for the calibrated **linear**, **linear2** and **calval2** algorithms are all very similar, as could be expected because they all mainly depend linearly on high frequency (especially 85 GHz) Tbs. The **barrett**, **ferraro** and **ferriday** algorithms do not fall into this category, which explains why the scatterplots for these algorithms are different from the "linear high frequency" algorithm scatterplots.

The rms errors for the single scene are smaller than those for the whole training set but the overall ranking of the algorithms stays the same: ("linear high frequency" best, **barrett** worst). The relatively poor performance of the **adler** algortihm is due to the large fraction of lower rain rates in this scene, which do not show a significant signature in the 85 GHz channel and thus can not be retrieved with the **adler** algorithm. Note that for this scene the rms errors for all but the **barrett** algorithm are within a range of less than 0.08 mm/hr ($\approx$ 6% of the mean).

Spatial and Temporal Sampling Errors

In this investigation we use the approach of [Kedem *et al.*, 1990] to analyzing the errors created by satellite sampling characteristics. The goal of that analysis was to study the coherence scale of rain rate data in time and space using different satellite sampling designs. This indicates how often a rain field should be sampled with satellite measurements so as to estimate the mean (monthly) area rain rate

with a given precision. The data set they used was the time series of rain radar observations obtained during GATE. Their analysis of samples from this space-time series showed that the frequency distribution of non-zero rain rates could be described by a lognormal probability function with parameters mean and standard deviation. Various sampling designs were then evaluated, using a minimum chi-squared estimator and the assumption of lognormal distributions, to determine how well they reproduced the mean rain rate (i.e. mean of the total distribution).

The analysis here is based on a subset of the AIP-2 FRONTIERS data set from 21 February (0:00) to 22 March (23:45). This time period contains a relatively high amount of coincident coverage by the radar and the F10 SSM/I sensor. The scenes are temporally spaced at 15 min intervals, and the grid spacing is 2.5 km. For the analysis of the spatial aspects alone, the scene shown in Figure 1.11a was selected.

Each satellite is characterized by a sampling design represented by the triple (t,x,y) with t = time sampling factor, and x,y = space sampling factors. Table 1.6 gives the sampling designs for the sensors investigated here. The 15 minute time interval and 2.5-km pixel spacing of the FRONTIERS data in the AIP-2 grid is assumed. The sampling design corresponding to the NOAA AVHRR instrument, for example, is specified by (48,1,1) which implies sampling every pixel every 12 hours (48 x 15 minutes). The AVHRR and Meteosat designs are included to compare the errors using microwave satellites with those of satellite systems presently used in operational rainfall estimation.

Table 1.6: Sampling Characteristics

Sensor	Design (t,x,y)	Time Offset (hrs)	FOV (km)
radar	(1,1,1)	0	1
AVHRR(LAC)	(48,1,1)	2, 7.5	2.5
Meteosat	(2,2,2)	0	7.5
MIMR (90 GHz)	(48,2,2)	6	4.9
SSM/I (85 GHz)	(48,5,5)	6	13
SSM/I (19 GHz)	(48,11,11)	6	43

Also given in Table 1.6 are the effective field-of-views (FOV) used in this analysis for the different sensors. For the microwave sensors it is the 3 dB beamwidth of the antenna pattern. To simulate the spatial averaging effect, a given scene is averaged with a box filter of width = FOV in the case of Meteosat, and with a 101 km x 101 km array containing normalized antenna pattern weights in the case of SSM/I and MIMR. Because of the 2.5-km grid spacing, the AVHRR is simulated with 2.5 km pixel size and spacing (rather than the nominal 1 km), and the 7.5 km FOV for Meteosat (5 km nominal value) is due to the minimum averaging filter of 3x3 pixels.

Comparisons are based on rain rate statistics (primarily rain probability and mean rain rate) derived from sample histograms. Given the time offset and the time sampling factor in the sampling design, the correct scene in the radar rainfield series is identified. The field is then averaged (if requried) and sampled at the sample

Table 1.7: Sampling Design Comparison

Design	Sampling Period	Probability (%)	⟨RR⟩ (mm/hr)
(1,1,1)	1 day	21.0	1.38
	30 days	11.3	1.57
(48,1,1)	1 day	16.7	1.05
	30 days	11.6	1.53
(2,2,2)	1 day	20.8	1.37
	30 days	11.3	1.56
(48,2,2)	1 day	25.9	1.49
	30 days	10.4	1.62
(48,5,5)	1 day	25.6	1.54
	30 days	10.3	1.66
(48,11,11)	1 day	28.6	1.42
	30 days	10.5	1.66

spacing of the given design. These samples are then accumulated over 1, 3, 7, 10, and 30 day periods and stored as histograms.

To derive sampling statistics we assume as in [Kedem *et al.*, 1990] that the actual rain rate distribution is a mixed distribution with two components: the continuous component of lognormal distributed non-zero rain rates and a discrete component at zero rain rate. The non-zero rain rate samples can therefore be characterized by the mean and standard distribution of the histograms of ln(RR), and the ratio of the number of non-zero to number of zero rain samples gives the rain probability. Time series of these sample statistics are used to determine how many days of observations are needed for the rain rate estimates of one satellite to approximate those of the radar data set or of another satellite sensor.

Sampling comparisons

Comparisons are first made of the sampling designs only. These results therefore represent the ideal measurement case of a 2.5-km wide box filter antenna pattern, and are equivalent to the actual sensor sampling only in the case of the radar and AVHRR (approximately). The sample statistics derived for periods of 1 and 30 days are presented in Table 1.7. After 1 day rain probabilities for satellite designs deviate from the actual value by up to 7.6%; after 30 days deviations for all designs are less than 1%. Likewise for the mean rain rate, after 30 days there is only at most 0.09 mm/hr deviation from the actual mean. These results would indicate that temporal averaging is effective in bringing satellite estimates into better agreement with actual rainfall statistics.

We now wish to consider the effect of spatial averaging by the satellite sensors. Table 1.8 presents statistics derived by sampling all points in a single scene averaged with sensor-appropriate filters as described above. They indicate a clear increase in rain probability and decrease in mean rain rate with increasing FOV. For the SSM/I 19 GHz sensor there is a factor of approximately 3 deviation from the actual

Table 1.8: FOV Comparison

Sensor	Probability (%)	<RR> (mm/hr)	RRmax (mm/hr)
radar	11.5	1.92	18.0
Meteosat	14.4	1.30	17.1
MIMR 90 GHz	14.4	1.29	17.1
SSM/I 85 GHz	21.1	0.80	12.2
SSM/I 19 GHz	31.2	0.59	6.1

Table 1.9: FOV + Spatial Sampling Comparison

Sensor	Probability (%)	<RR> (mm/hr)	RRmax (mm/hr)
radar	11.5	1.92	18.0
Meteosat	14.5	1.29	16.4
MIMR 90 GHz	14.4	1.29	16.6
SSM/I 85 GHz	21.2	0.80	10.6
SSM/I 19 GHz	29.7	0.59	5.9

value for all statistics. The identical statistics for Meteosat and MIMR 90 GHz are somewhat misleading because of the larger than actual FOV used in the Meteosat simulation.

Table 1.9 presents the statistics derived from the same scene where FOV averaging and spatial sampling have been combined. The results change very little from those where all points are sampled.

Integrating FOV averaging into the complete space-time sampling simulation produces the results given in Table 1.10. Comparison with Table 1.7 suggests that the effect of FOV averaging is to diminish the improvement won through sampling over longer periods. This is likewise indicated in the corresponding time series of rain probability and mean rain rate shown in Figures 1.6 to 1.8. For the optical sensors agreement with the radar data is reached after only 3 to 7 days. However even after 30 days the microwave sensors overestimate rain probability by 5 to 30% and underestimate mean rain rate by factors of 5 to 20. Based on sampling design alone (see Table 1.7), the microwave sensors should underestimate rain probability and overestimate mean rain rate. Note that the finer sampling and the higher resolution of the MIMR 90 GHz sensor combine to produce better agreeement with actual mean values than obtained with the SSM/I 85 GHz sensor.

Beam-filling error

The results presented above show that FOV-averaging is the most important limitation to obtaining valid rain statistics with microwave sensors. This averaging leads to the so-called beam-filling error due to three factors: (1) rain inhomogeneity within the sensor FOV; (2) nonuniform instrument sensitivity over the FOV (an-

Table 1.10: Sensor Sampling Comparison

Sensor	Sampling Period	Probability (%)	<RR> (mm/hr)
radar	1 day	21.0	1.38
	30 days	11.3	1.57
AVHRR	1 day	16.7	1.05
	30 days	11.6	1.53
Meteosat	1 day	29.9	0.70
	30 days	15.0	0.84
MIMR 90 GHz	1 day	46.7	0.30
	30 days	17.1	0.33
SSM/I 85 GHz	1 day	72.1	0.18
	30 days	28.8	0.10
SSM/I 19 GHz	1 day	87.4	0.19
	30 days	40.4	0.08

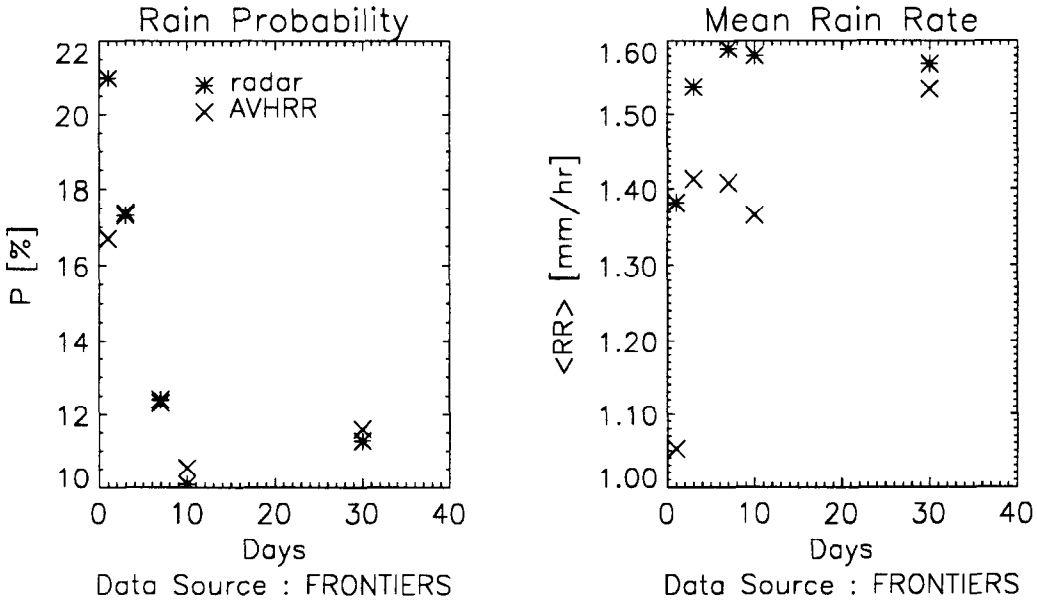

Figure 1.6: Time series of rain probability and mean rain rate for radar and AVHRR sampling characteristics.

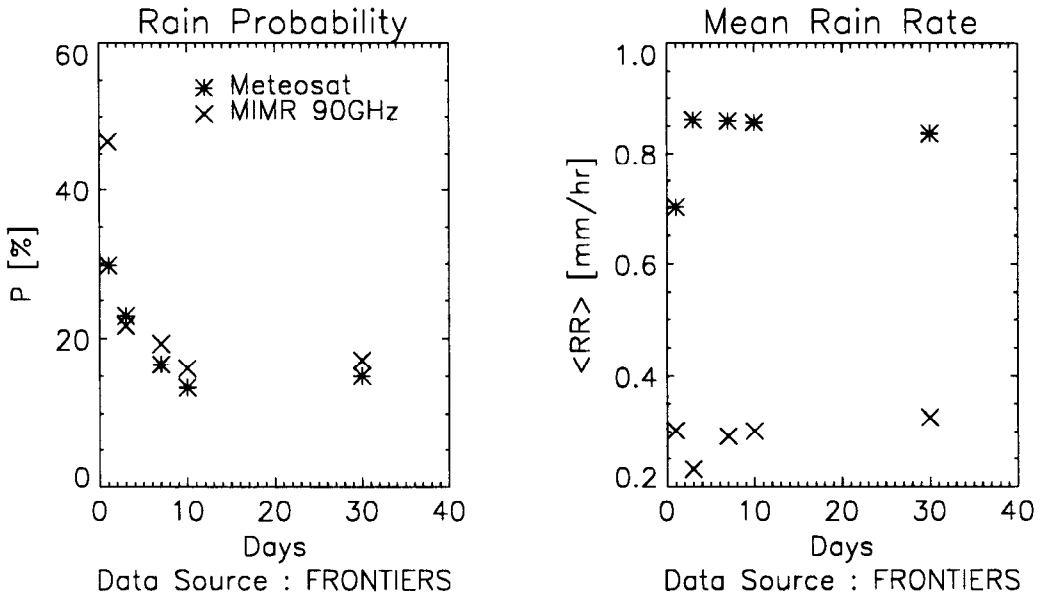

Figure 1.7: Time series of rain probability and mean rain rate for Meteosat and MIMR sampling characteristics.

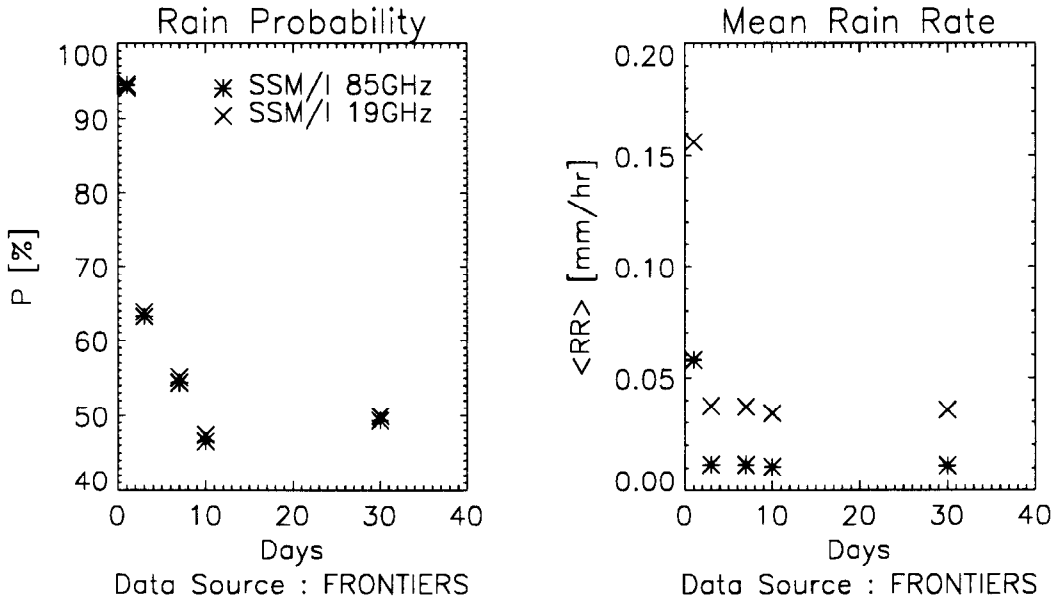

Figure 1.8: Time series of rain probability and mean rain rate for SSM/I 19 and 85 GHz sampling characteristics.

tenna pattern); and (3) nonlinear nature of the Tb-RR relationship, especially at the lower microwave frequencies. Additional errors in rain retrieval result because algorithms typically employ different combinations of channels (footprints of the SSM/I channels range from 13 km to 69 km) each of which averages over a slightly different area. That the rainfield typically is spatially inhomogeneous over the FOV can be seen by comparing Figures 1.11(a) and 1.11(b).

A major difficulty in estimating the beam-filling error is separating it from the total retrieval error. This was attempted analytically by Chiu *et al.* [1990] and Graves [1993] for single-channel algorithms. The expression derived by Chiu et al. for the beam-filling error consisted of two terms: one the variance of the rainfield and the other dependent on the nonlinearity of the Tb-RR relationship. Graves obtains a similar result and goes further to express rainfield variance in terms of the fractional area of the FOV raining per rain rate. Neither of these studies took account of antenna pattern weighting.

Short and North [1990], in their analysis of ESMR data, took a simulation approach to this problem based on applying a Tb-RR model to radar-derived rain rates and then averaging with appropriate antenna pattern weighting. The beam-filling error estimated therefore includes the effect that generally the area "seen" by the sensor (i.e. that falls within the antenna pattern) is larger than the nominal FOV over which the radar-derived rain rates are averaged. However it may also include errors due to a mismatch between assumptions of the algorithm applied and assumptions in the model.

In the analysis here we use a formulation similar to [Chiu *et al.*, 1990] to derive an expression for the beam-filling error. We consider a single frequency algorithm with a single value Tb-RR relationship which is generally valid for low rain rates. Let [Tb] be the measured brightness temperature (i.e. with antenna pattern weighting), and $\langle \mathrm{Tb} \rangle$ the average brightness temperature (uniform weighting) over the nominal pixel area. Then the estimated rain rate RR_e can be written in Taylor expansion about $\langle \mathrm{Tb} \rangle$ as

$$\begin{aligned} \mathrm{RR}_e([\mathrm{Tb}]) &= \mathrm{RR}(\langle \mathrm{Tb} \rangle) + \\ &\quad ([\mathrm{Tb}] - \langle \mathrm{Tb} \rangle) \cdot \mathrm{RR}'(\langle \mathrm{Tb} \rangle) + \\ &\quad ([\mathrm{Tb}] - \langle \mathrm{Tb} \rangle)^2 \cdot \mathrm{RR}''(\langle \mathrm{Tb} \rangle). \end{aligned} \tag{1.20}$$

Letting $\langle \mathrm{RR} \rangle$ be the average rain rate over the nominal area (the desired quantity) then the total retrieval error $\delta\mathrm{RR} = \mathrm{RR}_e - \langle \mathrm{RR} \rangle$, or

$$\begin{aligned} \delta\mathrm{RR} &= \mathrm{RR}(\langle \mathrm{Tb} \rangle) - \langle \mathrm{RR} \rangle + \\ &\quad ([\mathrm{Tb}] - \langle \mathrm{Tb} \rangle) \cdot \mathrm{RR}'(\langle \mathrm{Tb} \rangle) + \\ &\quad ([\mathrm{Tb}] - \langle \mathrm{Tb} \rangle)^2 \cdot \mathrm{RR}''(\langle \mathrm{Tb} \rangle). \end{aligned} \tag{1.21}$$

If the algorithm concept were perfect and the algorithm calibrated with representative data (as done above), δRR would result only from beam-filling errors. If in addition the rainfield were uniform, then $\delta\mathrm{RR} = 0$. For the more usual case of nonuniform rainfields, we can interpret the right hand side of Eqn. 1.21 as $(\mathrm{RR}(\langle \mathrm{Tb} \rangle) - \langle \mathrm{RR} \rangle)$ representing primarily the error due to the nonlinearity of the

Table 1.11: Beam-Filling Error δRR_w

Channel (GHz)	δRR_w (mm/hr)
85	-0.9 to +1.4
37	-3.5 to +1.6
22	-4.9 to +1.9
19	-5.5 to +2.0

Tb-RR relationship, and the other two terms expressing mainly the error resulting from spatially inhomogeneous rainfields, although the two factors are not completely separated.

For linear algorithms Eqn. 1.21 reduces to

$$\delta RR_w = a1 \cdot ([Tb] - \langle Tb \rangle) \tag{1.22}$$

showing that the beam-filling error for linear algorithms is not zero but equal to the difference between antenna pattern and uniform weighting over the footprint (hence the subscript w). For linear algorithms using N channels, it can be shown that

$$\delta RR_w = \frac{1}{N} \sum_i \delta RR_w(i), \quad i = 1, \ldots, N. \tag{1.23}$$

Correction of algorithm estimates

In general $\langle Tb \rangle$ is not known and δRR_w must be estimated either in a statistical sense by assuming a rainfall distribution function (e.g. [Short and North, 1990; Graves, 1993]) or with image statistics from the highest resolution channel [Wilheit and Chang, 1980]. This latter technique has recently been used by Kummerow and Giglio [1994] who took the variance in the 85 GHz channel as an indicator of storm system spatial variability. Empirical correction schemes for the beam-filling error also have been suggested such as that proposed by [Liu and Curry, 1992] based on the work of [Chiu *et al.*, 1990].

With the availability of coincident radar-derived rain rates it is possible here to calculate δRR_w directly by applying the inverse of the Tb-RR relationship to Eqn. 1.22, such that $\delta RR_w = [RR] - \langle RR \rangle$. This has been done for the scene shown in Figure 1.11 for all four SSM/I channels. As in Figure 1.11b $\langle RR \rangle$ is calculated for 25 km pixels. The results presented in Table 1.11 include both land and water areas. They indicate, as expected, increasing beam-filling error with increasing footprint size. They also show that the beam-filling error is not a simple bias in one direction: depending on whether the high intensity rain areas are nearer the center or nearer the edge of the nominal area, the error can be either positive or negative.

Because the expressions for δRR_w derived above are for linear algorithms, only correction of the algorithms **adler**, **smith**, **ferriday** and **calval** is considered. The rain rate estimates with these algorithms for SSM/I scene 910302.1850 were corrected using the radar-derived δRR_w for the coincident data points over land shown in Figure 1.11(b). For the **smith**, **ferriday** and **calval** algorithms, the expression for δRR_w in

Table 1.12: Algorithm Performance: Scene 910302.1850

	adler	calval	ferriday	smith
Recalibrated Algorithms				
rms	1.257	1.193	1.230	1.179
bias	0.326	0.385	-0.218	0.210
corr.	0.352	0.488	0.350	0.441
Corrected Algorithms				
rms	1.341	1.075	0.711	0.948
bias	0.305	0.868	0.264	0.693
corr.	0.211	0.872	0.888	0.873

Eqn. 1.23 was used, assuming the recalibrated **calval** algorithm to be approximately linear.

Table 1.12 gives the performance statistics before and after correcting for beam-filling. The correction had little or no effect on the **adler** algorithm results, as expected since the beam-filling error at 85 GHz is small. The effect on the other three algorithms is to reduce the rms error and increase the correlation between SSM/I and radar estimates. However an additional bias of $\approx +0.5$ mm/hr accompanies the correction.

Conclusions

Algorithms for rain retrieval over land with passive microwave imagers have been analyzed for possible errors due to variations in surface type and surface temperature and for errors resulting from sensor sampling characteristics. The algorithms investigated were taken from the AIP-2 and PIP-1 algorithm intercomparison projects, specifically those algorithms that are readily implemented with coefficients published in the literature.

For the purpose of evaluating algorithm sensitivity to variations in land emissivity and temperature, model brightness temperature data, generated with a radiative transfer routine for a number of stratiform and convective rain situations, were used. Considering different land surface types and temperatures, it was found that these surface variations have a much larger effect on both brightness temperatures and the rain retrieval results of most algorithms than do variations in the atmospheric parameters previously investigated. The effect of changing surface temperature is greatest on algorithms using a single channel (**adler**) or multiple channels additively (**smith**) with rain rate errors reaching over 10 mm/hr for a 10 K change in surface temperature. On the other hand, algorithms using channel differences (**ferriday**) can compensate for temperature effects very well (<3 mm/hr error for a 10 K change). Such algorithms cannot compensate for surface type variations, however, because the Tb variations for different channels are not of the same size. Results indicate that algorithms using the 85 GHz channel have the lowest sensitivity (<1mm/hr) to these variations. In future algorithms a channel with a frequency of 10 GHz or

below might help to estimate surface conditions and thus reduce the surface type effects on the retrieved rain rates.

These same algorithms were then applied to the SSM/I data from the AIP-2 and a statistical analysis of their performance carried out using the coincident FRONTIERS rain rates as "truth". The results showed large biases and rms errors in the retrieved rain rates because the data they were calibrated with were not representative for the data used in this study. Also "screening" (rain/no-rain) algorithms could not be applied successfully because of large ambiguities in the Tb signatures of rain and no-rain pixels. For this reason screening algorithms were not investigated further. Recalibration of the rain rate algorithms with the AIP-2 data set significantly improved algorithm performances. The relationship between averaged radar rain rate and brightness temperature for this data set was best represented by a linear combination of the 37 and 85 GHz channels; including the 19 and 22 GHz Tb in the retrieval process only slightly improved the retrievals. With this algorithm rms errors in retrieval of rain rate averaged over a 12.5 km radius SSM/I footprint could be reduced to 1.3 mm/hr.

Investigation of the error due to the spatial and temporal sampling characteristics of PMIs was carried out on a subset of the AIP-2 radar-derived rain rates covering a one month period. A comparison of the sampling designs of several satellite sensors, including Meteosat, AVHRR, SSM/I and MIMR, showed that if resolutions were all alike all sensors would produce very similar rainfall statistics (rain probability and mean rain rate) after one month of observations. However, when the effect of averaging over the FOV is included in the sampling analysis, sensors doing spatial averaging overestimate rain probability and underestimate mean rain rate even after 30 days of temporal averaging. The SSM/I 19 GHz sensor underestimated the mean rain rate of the radar data set by a factor of 20; based on its sampling design alone (no spatial averaging) it should only slightly overestimate the mean by a factor of 1.1. Slight improvement over SSM/I in estimating mean rain rate was seen by going to the denser sampling and higher resolution planned for the 90 GHz MIMR channel.

FOV averaging is therefore the most important limitation to obtaining valid rain statistics with microwave sensors. The result of FOV-averaging on rain rate retrievals is the beam-filling error. It was shown that even for linear algorithms a beam-filling error exists due to nonuniform instrument response over areas of inhomogeneous rain intensity. This error also varies in sign depending on the actual distribution of rain events within the FOV. Correction of algorithm results for this beam-filling effect improved retrieval results but not as much as regional calibration.

In addition to testing the effectiveness of regional calibration of rain retrieval algorithms on other areas and in other seasons, further research in this area should be done on the use of lower frequencies to be available on MIMR to compensate for surface type related error in rain retrievals over land, and incorporation of beam-filling correction into rain retrieval algorithms.

References

Adler, R. F., A. J. Negri, P. F. Keehn, and I. M. Hakkarinen, Estimation of Monthly Rainfall over Japan and Surrounding Waters from a Combination of Low-Orbit Microwave and Geosynchronous IR Data. *Journal of Applied Meteorology*, **32**(2), 335–356, 1993.

Allam, R., G. Holpin, P. Jackson, and G.-L. Liberti, Second Algorithm Intercomparison Project of the Global Precipitation Climatology Project AIP-2. Pre-Workshop Report, 1993.

Basili, P., P. Ciotti, G. d'Auria, F. S. Marzano, N. Pierdicca, and A. Mugnai, A precipitaion retrieval algorithm by space-borne multispectral radiometry based on cloud radiation models and multivariate techniques. *In preparation.*, 1993.

Bell, T. L., A. Abdullah, R. L. Martin, and G. R. North, Sampling errors for satellite-derived tropical rainfall: Monte Carlo study using a space-time stochastic model. *J. Geophys. Res.*, **95**, 2195–2205, 1990.

Browning, K., The FRONTIERS plan: a strategy for using radar and satellite imagery for very short-range precipitation forecasting. *Meteor. Mag.*, **108**, 161–184, 1979.

Burns, B. A., G. Heygster, and K. Künzi, Evaluation of Algorithms for Retrieval of Rain Rate with Passive Microwave Radiometers. Final Report, ESA/ESTEC Purchase Order 120419, 1993.

Burns, B. A., and F. Flender, Sensitivity of SSM/I Rain Rate algorithms to Variations in Water Vapour and Cloud Liquid Water – A Modeling Study. In *Specialist Meeting on Microwave Radiometry and Remote Sensing of the Environment*, 1994.

Chiu, L. S., G. R. North, D. A. Short, and A. McConnell, Rain estimation from satellites: Effect of finite field of view. *J. Geophys. Res.*, **95**, 2177–2185, 1990.

Collier, C. G., International radar networking. *Meteor. Mag.*, **121**, 221–239, 1992.

Colwell, R. N., editor, *Manual of Remote Sensing.* American Society of Photogrametry, Falls Church, VA, 2nd edition, 1983. pp. 196–197.

Deirmendjan, D., Scattering and polarization properties of water clouds and hazesin the visible and infrared. *Appl. Optics*, **3**, 187, 1964.

Goldhirsh, J., and B. H. Musiani, Dimension statistics of rain cell cores and associated rain rate isopleths derived from radar measurements in the mid-atlantic coast of the United States. *IEEE Trans. Geosci. Remote Sens.*, **30**, 28–37, 1992.

Graves, C. E., A model for the beam-filling effect associated with the microwave retrieval of rain. *J. Atmos. Oceanic Technol.*, **10**, 5–14, 1993.

Grody, N. C., Classification of Snow Cover and Precipitation Using the Special Sensor Microwave Imager. *Journal of Geophysical Research*, **96**(D4), 7423–7435, 1991.

Kedem, B., L. S. Chiu, and G. R. North, Estimation of mean rain rate: Application to satellite observations. *J. Geophys. Res.*, **95**, 1965–1972, 1990.

Kniveton, D. R., C. Kidd, E. C. Barrett, B. Motta, F. LaFontaine, M. Smith, and M. Goodman, WetNet PIP-1 Results Version 2, 1994.

Kummerow, C., and L. Giglio, A passive microwave technique for estimating rainfall and vertical structure information from space, Part I: Algorithm Description. *Journal of Applied Meteorology*, **33**, 3–18, 1994.

Liberti, G. L., Review of the SSM/I-based algorithms submitted for the GPCP-AIP/2. In *Proceedings of the Specialist Meeting on Microwave Radiometry and Remote Sensing of the Environment, Rome 14–17 February 94*, 1994.

Liu, G., and J. Curry, Retrieval of precipitation from satellite microwave measurement using both emission and scattering. *J. Geophys. Res.*, **97**, 9959–9974, 1992.

Mätzler, C., Algorithms for retrieving snowpack properties from a Multichannel Imaging Microwave Radiometer (MIMR), Study of Microwave Interaction with the Earth's Surface. Report, ESA Study Contract No. 8447/89/NL/PB/(SC), 1990.

Olson, W., F. LaFontaine, W. Smith, R. Merrill, B. Roth, and T. Achtor, Precipitation Validation. In Hollinger, J. P., editor, *DMSP Special Sensor Microwave/Imager Calibration/Validation, Final Report Vol II*, Naval Research Laboratory, Washington D.C., 1991.

Rogers, R. R., and M. K. Yau, *A Short Course in Cloud Physics*. Pergamon Press, 1991.

Sekon, R. S., and R. C. Srivaastava, Doppler radar observations of drop-size distributions in a thunderstorm. *Journal of Atmospheric Sciences*, **28**, 983–994, 1971.

Shin, K. S., and G. R. North, Sampling Error Study for Rainfall Estimate by Sattelite Using a Stochastic Model. *Journal of Applied Meteorology*, **27**, 1218–1231, 1988.

Short, D. A., and G. R. North, The beam filling error in the Nimbus 5 Electronically Scanning Microwave Radiometer observations of Global Atlantic Tropical Experiment rainfall. *J. Geophys. Res.*, **95**, 2187–2193, 1990.

Smith, E. A., A. Mugnai, H. J. Cooper, G. J. Tripoli, and X. Xiang, Foundations for Statistical-Physical Precipitation Retrieval from Passive Microwave Satellite Measurements. Part I: Brightness-Temperature Properties of a Time dependent Cloud Radiation Model. *Journal of Applied Meteorology*, **31**(6), 506–531, 1992.

Spencer, R. W., H. M. Goodman, and R. E. Hood, Precipitation Retrieval over Land with the SSM/I: Identification of the Scattering Signal. *Journal of Atmospheric and Oceanic Technology*, **6**, 254–273, 1989.

Wilheit, T. T., and A. T. C. Chang, An algorithm for retrieval of ocean surface and atmospheric parameters from the observations of the scanning multichannel microwave radiometer. *Radio Science*, **15**, 525–544, 1980.

WMO, Workshop Report on the Global Precipitaion Climatology Project (GPCP) Second Algorithm Inetrcomparison Project (AIP-2) August 1993, 1994.

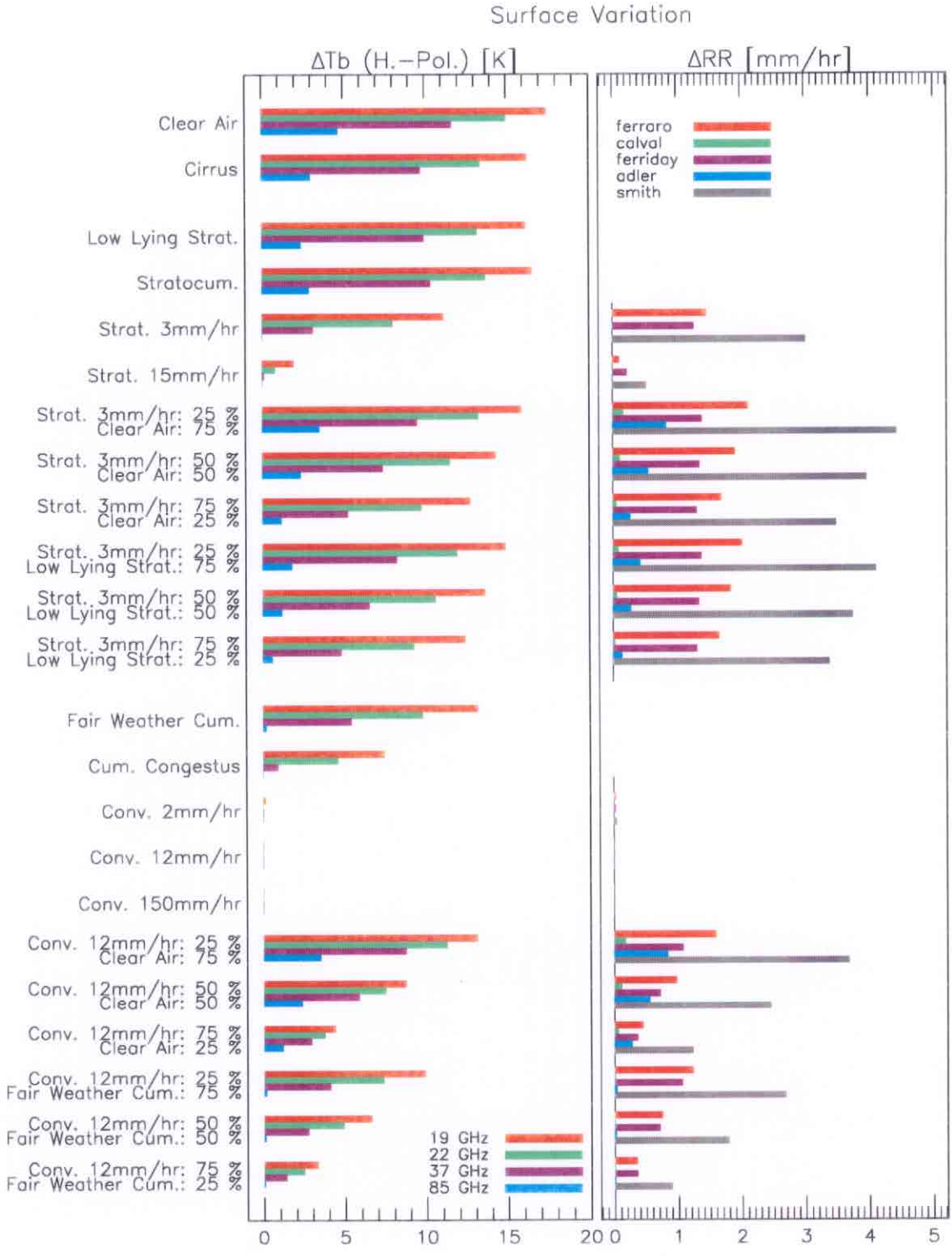

Figure 1.9: Changes in brightness temperature and rain rates due to surface type variation.

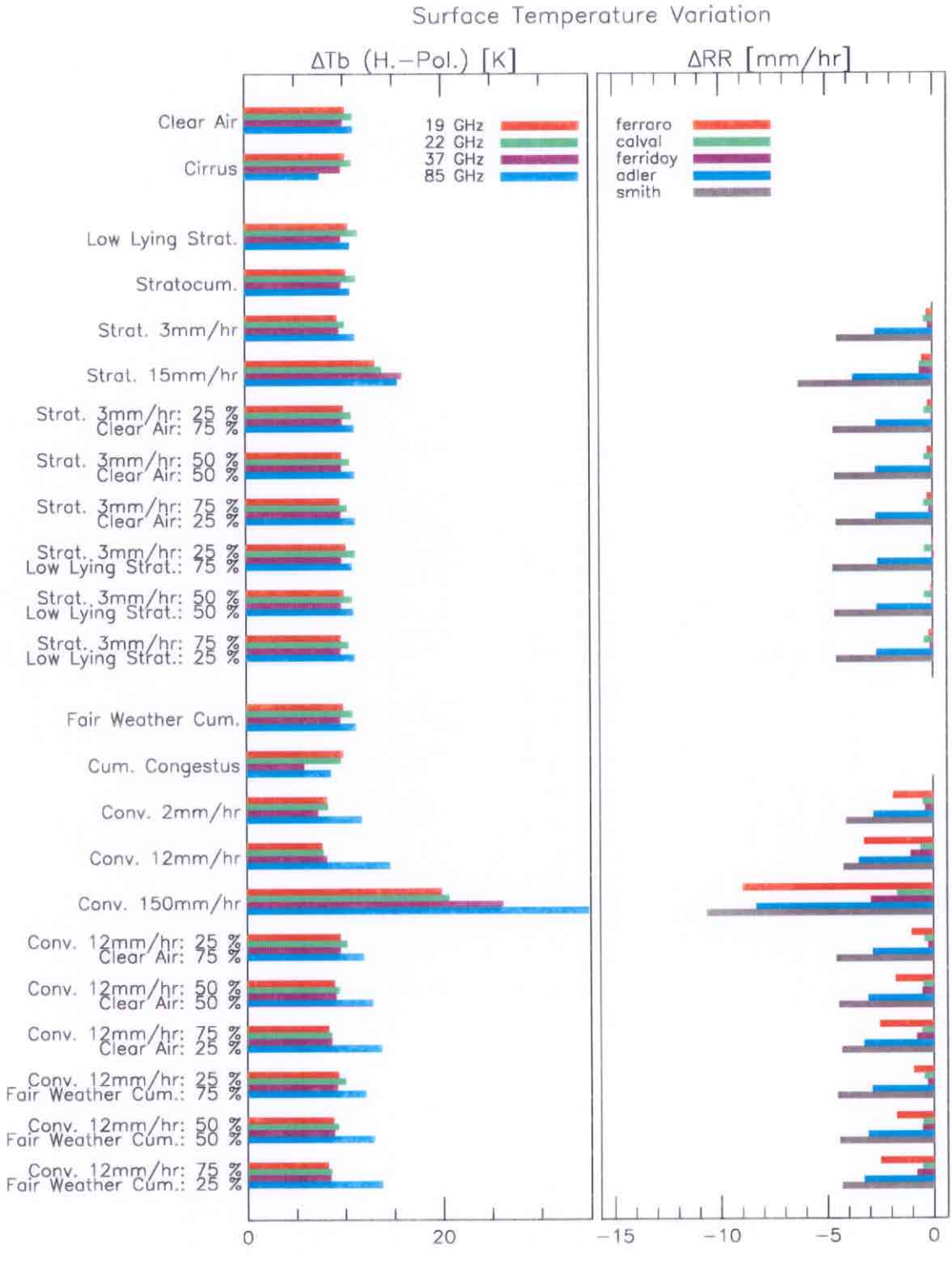

Figure 1.10: Changes in brightness temperatures and rain rates due to surface temperature variation.

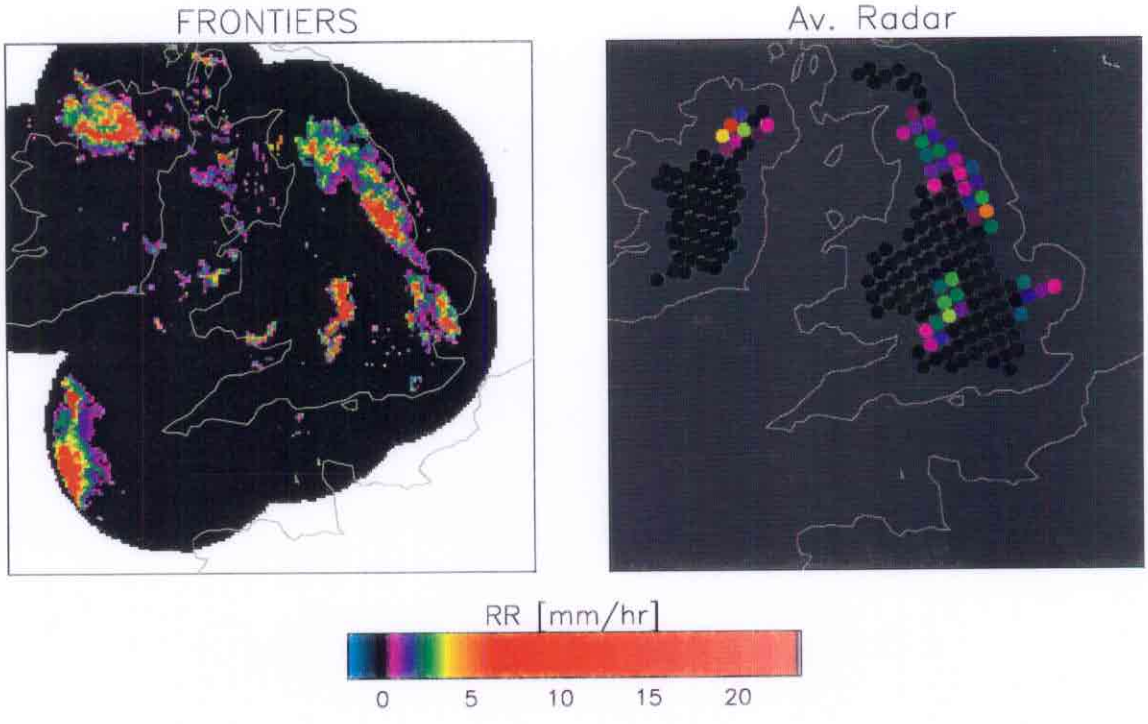

Figure 1.11: FRONTIERS rain rates for scene 910302.1850 (a) in 2.5 km AIP-2 grid, and (b) averaged over a 25 km diameter area at coincident SSM/I pixel positions.

Part 2

Image Restoration Techniques for Improving SSM/I Spatial Resolution

Introduction

Satellite Passive Microwave Imagers (PMI) are currently being used to obtain information on geophysical quantities important to the hydrologic cycle. Because of their broad swath and relatively frequent overpasses, these satellite sensors can provide estimates of such quantities as rain rate, cloud liquid water, and atmospheric water vapor on spatial and temporal scales compatible with regional weather prediction and global climate models. Such measurements are of greatest importance over the ocean where in situ observations are sparse.

However, because rain fields and clouds can be patchy on scales much smaller than the field-of-view (FOV) of the PMI, large errors can occur in estimating these parameters when only part of the FOV contains rain or cloud. This is called the beam-filling error, and errors in rainfall estimates as large as 50% have been observed with data from the ESMR instrument obtained during the GARP Atlantic Tropical Experiment (GATE) [Short and North, 1990]. And although data channels with higher frequencies (37 and 85 GHz), and therefore smaller FOV's, are available on present PMIs, most algorithms for rain retrieval over ocean still depend heavily on the 19 GHz channels. This means that the effective spatial resolution of the retrieval results is limited by the FOV of the 19 Ghz channel: approximately 60 km for SSM/I and 20 km (design) for MIMR.

One possible means of reducing the beam-filling error is to apply post-processing techniques that improve the effective resolution of the passive microwave data, at least to the extent that all channels used in the rain retrieval algorithms have similar FOVs. The purpose of this paper is to investigate the application of deconvolution methods for this purpose.

The typical imaging process in remote sensing involves 'optics' with non-delta function response characteristics and finite receiver noise such that the resulting image is blurred and corrupted in some manner. The objective of image restoration is to reduce this degradation, making the restored image as close as possible to

the observed scene. This can be done if the antenna pattern is known so that the imaging process can be modeled.

The next section describes the imaging model as well as the restoration techniques that have been examined. These techniques, a signal adaptive least squares algorithm, two entropy based methods as well as the commonly used Wiener filter and constrained least squares restoration are first applied to test data where both the original image and the degradation process are known exactly. Sample applications to SSM/I data are then presented, and the results are evaluated by comparing rain rates derived from restored and unrestored SSM/I data to radar rain rates.

Description of Techniques

Modelling the imaging system

Letting p and q be the row (along scan) and column (along track) indices in the image domain, the actual brightness temperature distribution (true image) $f(p,q)$ is related to the measured antenna temperatures $d(p,q)$ by a Fredholm integral equation of the first kind. In the discrete case this reduces to the sum

$$d(p,q) = \sum_{i=0}^{M-1} \sum_{j=0}^{N-1} f(i,j)\, h(p,q,i,j) + n(p,q) \tag{2.1}$$

where $h(p,q,i,j)$ is the antenna pattern and $n(p,q)$ the noise originating from the amplifier as well as from the physical signal. The task of image restoration is to determine $f(p,q)$ from $d(p,q)$.

Traditional image restoration techniques are in most cases applied in the frequency domain which makes the restoration much faster. These techniques presume a linear shift-invariant (LSI) degradation, where the antenna pattern, or more correctly speaking, the point spread function, is dependent only on the coordinate differences $(p-i, q-j)$ instead of all four coordinates. In this case Eq.(2.1) takes the form

$$d(p,q) = \sum_{i=0}^{M-1} \sum_{j=0}^{N-1} f(i,j)\, h(p-i,q-j) + n(p,q) \quad . \tag{2.2}$$

When performing the restoration in the space domain, we need not to make this assumption.

Wiener Filter

The Wiener Filter is well known in the signal processing literature [Gonzales and Woods, 1992; Jain, 1989; Lim, 1990]. It considers the true image $f(p,q)$ and the noise $n(p,q)$ as realizations of two signal generating stochastic processes and minimises the restoration errors

$$E\left\{[f(p,q) - \hat{f}(p,q)]^2\right\} \rightarrow \min. \tag{2.3}$$

with $\hat{f}$ the estimate of f and $E\{\ldots\}$ the expectation value of the random variable in the brackets.

The Wiener Filter can be derived from Eq.(1.3) as in Lim [1990]:

$$\hat{F}(k,l) = \frac{D(k,l)}{H(k,l)} \cdot \frac{|H(k,l)|^2}{|H(k,l)|^2 + \Gamma(k,l)} \tag{2.4}$$

where

$$\Gamma(k,l) = \Phi_{nn}(k,l)/\Phi_{ff}(k,l) \ . \tag{2.5}$$

$\Phi_{nn}(k,l)$ and $\Phi_{ff}(k,l)$ are the power spectral density functions of $n(p,q)$ and $f(p,q)$, respectively. $\Gamma(k,l)$ is the inverse signal-to-noise ratio of the image $(1/SNR)$ and can be estimated from the data. Alternatively, a constant value for $\Gamma(k,l)$ can be evaluated empirically [Wahl, 1989].

Constrained Least Square Filter (CLS)

The constrained filter (Constrained Least Squares filter, CLS) minimises the convolution of the estimate $\hat{f}(p,q)$ with a regularization function $c(p,q)$, with the goal to obtain an estimation $\hat{f}$ as smooth as possible:

$$\sum_{p=0}^{M-1} \sum_{q=0}^{N-1} \left[c(p,q) * \hat{f}(p,q) \right]^2 \rightarrow \min. \tag{2.6}$$

under the constraint

$$\sum_{p=0}^{M-1} \sum_{q=0}^{N-1} \left[d(p,q) - h(p,q) * \hat{f}(p,q) \right]^2 = E_n \ , \tag{2.7}$$

where $c(p,q)$ is a discrete approximation to the first or second derivative. Here, $*$ is the convolution symbol and the noise power E_n enters in the restoration process as *a priori* knowledge.

The minimization problem can be solved by using the method of Lagrange multipliers

$$\sum_{p=0}^{M-1} \sum_{q=0}^{N-1} [c(p,q) * \hat{f}(p,q)]^2 + \lambda \sum_{p=0}^{M-1} \sum_{q=0}^{N-1} [d(p,q) - h(p,q) * \hat{f}(p,q)]^2 \longrightarrow \min. \tag{2.8}$$

where λ is the so called Lagrange multiplier. Eq.(2.8) can be solved in the frequency domain:

$$\hat{F}(k,l) = Q(k,l) \cdot D(k,l) \ . \tag{2.9}$$

The filter $Q(k,l)$ can be written as [Wahl, 1989]

$$Q(k,l) = \frac{1}{H(k,l)} \frac{\lambda |H(k,l)|^2}{|C(k,l)|^2 + \lambda |H(k,l)|^2} \tag{2.10}$$

where $\hat{F}(k,l)$, $D(k,l)$, $H(k,l)$ and $C(k,l)$ are the two-dimensional Fourier transforms of $\hat{f}(p,q)$, $d(p,q)$, $h(p,q)$ and $c(p,q)$, respectively. The filter function $Q(k,l)$ is therefore composed of an inverse filter multiplied with a regularization filter.

The noise dependent parameter λ controls the regularization and must be estimated from the data. In the case of high noise energy, λ must be small to emphasize the regularization. In the case of absence of any noise, a large value of λ turns Eq.(2.10) into a inverse filter. Note that the regularization part suppresses high frequencies.Therefore, the choice of λ is always a compromise between resolution improvement and reduction of noise amplification.

Adaptive Constrained Least Squares Restoration (ACLS)

In order to reduce the noise amplification of regions in the image with low local standard deviation and to improve the resolution of regions with high local standard deviation (e.g. edges), Bundschuh [1991] presented the idea of a signal adaptive algorithm by rewriting Eq.(2.6) as

$$\sum_{p=0}^{M-1}\sum_{q=0}^{N-1} w(p,q)[c(p,q) * \hat{f}(p,q)]^2 \longrightarrow \min \tag{2.11}$$

with an additional signal dependent weighting function $w(p,q)$. Minimizing Eq.(2.11) constrained by Eq.(2.7) yields

$$\sum_{p=0}^{M-1}\sum_{q=0}^{N-1} w(p,q)[c(p,q) * \hat{f}(p,q)]^2 + \lambda \sum_{p=0}^{M-1}\sum_{q=0}^{N-1}[d(p,q) - h(p,q) * \hat{f}(p,q)]^2 \longrightarrow \min \tag{2.12}$$

For the regularization function $c(p,q)$ the first derivative is used. The partial derivatives are approximated by the sum of the differences of neighboring pixels in the x- and y-directions, respectively. Analogously, the weighting function $w(p,q)$ is split into the sum of two directional components w_x and w_y:

$$\begin{aligned} &\sum_{p=0}^{M-1}\sum_{q=0}^{N-1} w_x(p,q)\left(\hat{f}(p,q) - \hat{f}(p-1,q)\right)^2 \quad + \\ &\sum_{p=0}^{M-1}\sum_{q=0}^{N-1} w_y(p,q)\left(\hat{f}(p,q) - \hat{f}(p,q-1)\right)^2 \quad + \\ &\lambda \sum_{r=0}^{M-1}\sum_{s=0}^{N-1}\left[d(r,s) - \sum_{p=0}^{M-1}\sum_{q=0}^{N-1}\hat{f}(p,q)\,h(r-p,s-q)\right]^2 \longrightarrow \min \end{aligned} \tag{2.13}$$

The signal dependent weighting function $w(p,q)$ can be calculated from the data. In regions with small local standard deviation, the weighting function must have high values to emphazise the regularization, whereas at edges the weighting function should reduce the influence of the smoothness criterion in order to improve the resolution. The weighting function is essentially the normalized inverse of the first derivative of $\hat{f}(p,q)$ [Hunewinkel, 1993]. Since the weighting function introduces nonlinearity into Eq.(2.11), the resulting Eq.(2.13) must be solved in the spatial domain iteratively using the Gauß-Seidel Algorithm [Press *et al.*, 1992].

Maximum Entropy Restoration

The premise of maximum entropy restoration is that the best result is that with the highest probability with respect to the imaging system and the measured data. This can be achieved by maximizing the entropy of the restored image

$$S = -\sum_{p=0}^{M-1}\sum_{q=0}^{N-1}\hat{f}(p,q)\ln(\hat{f}(p,q)). \tag{2.14}$$

The idea is attributed to Jaynes [1982]. According to his imaging model an image measures the luminance at each pixel and each luminance quantum has an equal *a priori* chance of appearing at any pixel. If any two distributions have the same probability, the one with the most possible configurations is the most probable. Maximization of Eq.(2.14) constrained by Eq.(2.7) can be written as

$$-\sum_{p=0}^{M-1}\sum_{q=0}^{N-1}\hat{f}(p,q)\ln(\hat{f}(p,q))+\lambda\sum_{p=0}^{M-1}\sum_{q=0}^{N-1}[d(p,q)-h(p,q)*\hat{f}(p,q)]^2 \longrightarrow \max \quad (2.15)$$

Because of the nonlinearity introduced by the entropy maximization term, a closed solution of Eq.(2.15) is not known. Many researchers have presented algorithms to solve Eq.(2.15). In particular Skilling [1985], Skilling [1989], Skilling [1990], Gull [1985], Gull [1989] have developed a software package, known as MemSys5, which has become important in restoration of astrophysical images. A variation on this standard algorithm is based on an idea of Kao [Gonsalves and Kao, 1987; Gonsalves *et al.*, 1987], who formulated an algorithm (Kao) similar to the Wiener filter with an additional entropy maximizing term.

Backus-Gilbert Restoration and Interpolation

Recently several papers have been published using Stogryn's [Stogryn, 1978] application of the Backus-Gilbert inversion [Backus and Gilbert, 1970] to passive microwave data for image restoration and interpolation. Poe [1990] proposes an interpolation procedure which attempts to maintain the characteristics of the original data (resolution and antenna pattern) in the interpolated values. Although resolution improvement was not the goal of the algorithm, fine details in the SSM/I 85 GHz images shown are clearly better distinguishable. Farrar and Smith [1992] use the Backus-Gilbert formalism to obtain a single optimum resolution for all SSM/I channels. This is necessary if an inversion algorithm uses different frequencies and therefore different resolutions simultaneously. The trade-off between resolution improvement and noise amplification is controlled by setting a tuning parameter γ and by maximizing the inter-channel correlation. In the examples presented γ is determined for each image individually. The optimization criterion does not take into account the physically different conditions at the different frequencies which lead to frequency- dependent details. On the contrary it tends to make the images of different frequencies more uniform.

Rather than attempt to obtain "optimum" resolution for all channels, Robinson *et al.* [1992] standardize the resolution of the 19-, 22- and 85-GHz channels to that of the 37 GHz channel, but for the same reasons as Farrar and Smith. Both Poe [1990] and Robinson *et al.* [1992] agree that improving the resolution of the 37- and 85 GHz-channel is not possible, but on different grounds. Whereas Poe, like Sethmann [1992], observes the effects of undersampling, for Robinson et al. the problem is noise amplification. In the latter the tuning parameter γ is determined from the results of a test image which had been blurred with the antenna characteristic and had channel-specific noise superimposed before restoration.

The Backus-Gilbert method used here is that from Robinson *et al.* [1992]. The routine was obtained as part of rain retrieval software from C. Kummerow (NASA Goddard).

Application to Test Images

The five deconvolution algorithms described above have been implemented and a systematic comparison carried out on test data. The test images are derived from the Landsat image shown in Figure 2.3. This scene shows the harbor area of Bremerhaven, Germany, and exhibits sufficient detail and contrasts by which to judge resolution improvement.

Image degradation is done by adding Gaussian noise and smoothing with filters having Gaussian or box characteristics. The Gauss filters are characterized by standard deviations of $\sigma = 2$ and 5. The box filters used have dimensions 5×5 and 7×7 pixels. The blurred images were corrupted with normally distributed noise with standard deviations $\sigma_n = 1, 2$ and 5. In this way a total of twelve test images were generated. Note that the degradation using the Gauss filter with $\sigma = 2$ and noise standard deviation of $\sigma_n = 1$ is most similar to the SSM/I case.

Figure 2.4 shows the degraded and restored images for the case with distortion characteristics most similar to SSM/I. The Wiener filter restorations show little and the CLS restoration more ringing near edges; the ACLS restoration seems somewhat blocky. The two maximum entropy restorations are noisy. The MemSys5 restoration shows rough and the Kao restoration fine noise.

Figure 2.1 demonstrates the relative performances with a profile through the image. Due to its signal adaptive character, the ACLS algorithm reduces the noise amplification in flat regions and improves the resolution at edges. Note the strong noise amplification of the entropy-based algorithms. This figure also shows that the ACLS filter produces much less but still visible overshooting near edges and peaks than the CLS filter.

To quantify resolution improvement, three measures have been calculated: the normalized mean square error (Δ_{MSE}), change in signal-to-noise ratio Δ_{SNR} evaluated in the space domain, and change in edge steepness s_{rest}.

Since the original image is available, the restoration performance can be measured using the ratio of the mean square errors

$$\Delta_{MSE} = 10 \cdot \log_{10} \left(\frac{||d(p,q) - f(p,q)||^2}{||\hat{f}(p,q) - f(p,q)||^2} \right) \quad , \tag{2.16}$$

with $||\ldots||^2 = \sum\sum[\ldots]^2$ where the sum extends over the whole image. The quantity Δ_{MSE} indicates in decibels to what degree the restoration was able to compensate for the degradation. Therefore a larger Δ_{MSE} is obtained for a better restoration. In contrast to the quality measures discussed below, Δ_{MSE} is a global characterization of the restoration. It refers to the entire image and not to specific regions or pixels.

The noise amplification in space domain Δ_{SNR} can be written as

$$\Delta_{SNR} = 10 \cdot \log_{10} \left(\frac{\sigma_{\text{rest}}}{\sigma_{\text{deg}}} \right) \tag{2.17}$$

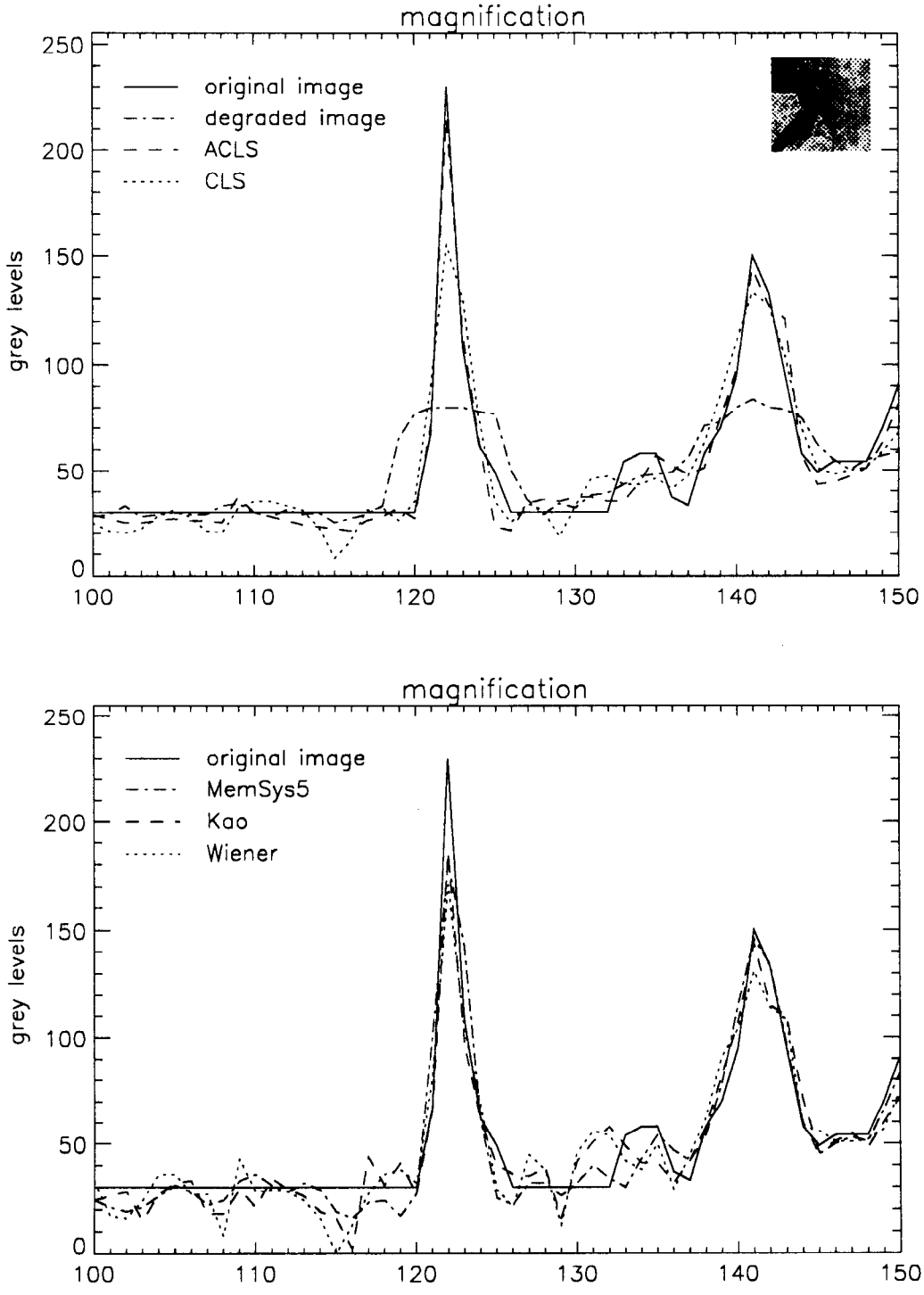

Figure 2.1: Profile through Landsat image. Top: comparing restoration results from the two least squares techniques to the original image. Bottom: comparing Wiener filter and maximum entropy methods to the original image.

where σ_{rest} and σ_{deg} represent the standard deviation of pixel values derived from subareas of low standard deviation in the restored and degraded images :

$$\sigma_{\text{rest}} = \left\langle \left(\left\langle \hat{f}(p,q) \right\rangle_{sub} - \hat{f}(p,q) \right)^2 \right\rangle_{sub} \tag{2.18}$$

and

$$\sigma_{\text{deg}} = \left\langle \left(\langle d(p,q) \rangle_{sub} - d(p,q) \right)^2 \right\rangle_{sub} \tag{2.19}$$

where $\langle x \rangle_{sub}$ means the average of the quantity x over the subarea sub of the image. A subarea of 8306 pixels was chosen from the inner region of the Weser river in the "Bremerhaven" scene where in the original image the standard deviation is equal to zero.

A steepness parameter s_{rest} is defined to measure the actual resolution improvement. For this purpose, a Gaussian fit to a profile through an edge was made in the restored and in the degraded image. The ratio of the standard deviations characterizing the two Gaussians (σ_{rest} and σ_{deg}) is used as a measure of the resolution improvement:

$$s_{\text{rest}} = \frac{\sigma_{\text{deg}}}{\sigma_{\text{rest}}} \tag{2.20}$$

σ_{rest} and σ_{deg} can be used also to calculate the actual resolution achieved. The ability of a system to resolve two closely separated point sources, the two-point resolution, is defined according to the so-called Rayleigh criterion in optics as the minimum distance which two point sources must be separated so that they are barely resolved under incoherent illumination. This is the case when the Airy disk generated by one source falls on the first zero of the Airy disk generated by the second. The resultant image intensity then shows a central dip which is about 81 % of the adjacent maxima [Goodman, 1968]. Translating this criterion by analogy to two neighboring Gaussian shapes with equal standard deviations σ, one finds that a separation of

$$\delta = 2.64\,\sigma \tag{2.21}$$

is necessary for the central minimum to be 81 % of the maxima. The highest meaningful resolution in a digital image is $\delta = 2$ because according to the sampling theorem peaks closer than this cannot be represented in a sampled grid.

The two-point resolution can also be characterized by the width a where the image of an ideal point source has dropped off to 3 dB. If again the point image is modeled as a Gaussian function, the 3 dB width a is related to the standard deviation σ of the Gaussian by

$$a \approx 2.353\,\sigma \approx 0.891\,\delta. \tag{2.22}$$

The 3 dB width a is therefore a good approximation within 11 % of the Rayleigh-criterion in optics, if the Airy disc may be modeled as a Gaussian function instead of the mathematically correct Bessel function $J_o(x)$.

Table 2.1 presents the average values of the quality measures obtained for the twelve degraded test images. The results for the Δ_{MSE} indicate that the ACLS algorithm produces the best overall improvement of the blurred images. The errors

Table 2.1: Mean Values of Restoration Quality Measures

Image: Landsat — Bremerhaven

Quality Measure	Restoration Algorithm				
	Wiener	CLS	ACLS	Kao	MEMSYS5
Δ_{MSE} [dB]	2.88	2.66	3.56	2.86	2.66
rank	2	4	1	3	4
edge steepness improvement	1.90	1.80	2.49	2.10	2.21
rank	4	5	1	3	2
noise amplification [dB]	4.30	2.82	2.00	4.55	3.06
rank	4	2	1	5	3

due to overshooting (seen in Figure 2.1) therefore affect the global image quality very little. As next best method is the Wiener filter which is slightly better than the Kao maximum entropy algorithm. The less satisfactory results from the maximum entropy techniques do not warrant the factor of 100 greater computation time they require.

The results for noise amplification in the spatial domain presented in Table 2.1 show that again the ACLS filter performs best. This is not surprising because due to its local adaptivity, the filter smooths more than it sharpens in this region where the grey-level variance in the degraded image originates only from the additive noise. In general the noise amplification decreases monotically with increasing standard deviation σ_n of the added noise and increases with the width of the low-pass filter. In the "SSM/I-case" (Gauss low-pass with $\sigma = 2$ and additive noise with $\sigma_n = 1$) the ACLS filter amplifies the noise by the factor 1.74. The ranking of the investigated filters, averaged over all cases considered, indicates that after the ACLS filter, the next best are the CLS and the MemSys5 filters, while the Kao and Wiener filter show the poorest performance.

The edge steepness improvement averaged over all cases for each considered filter is also given in Table 2.1. As the ACLS method is locally adaptive, the results for this filter are only valid locally exactly at the edge point considered. In low standard deviation regions the edge improvement is less. For the other filters, the steepness improvement is valid globally in the entire image. The larger the width of the low-pass filter, the greater is the steepness improvement parameter. In all cases the ACLS filter delivers the largest edge steepness improvement. The two maximum entropy filters Kao and MemSys5 show the next best and similar results, whereas the Wiener filter and the CLS filter give the poorest performance.

Application to PMI Data

In the application of restoration methods to the Landsat test image, the relative geometry of data samples is assumed to be defined by their pixel positions. This is not the case for data from the SSM/I or the planned MIMR which are conical scan instruments rotating continuously about the vertical axis. (For more details on the SSM/I instrument see [Hollinger *et al.*, 1990]). Due to this conical scanning the

relative geometry of samples changes over the scan and is no longer represented by relative pixel position in the image. In order to restore PMI data, this locally varying geometry must be accomodated, meaning that a linear shift variant restoration task must be performed.

Sethmann *et al.* [1994] examined this problem for restoration algorithms applied in the frequency domain. Their preferred solution is a geometric adaptive procedure where the measured image is restored once with each of the 64 antenna patterns adapted to the geometry corresponding to the each scan position. The result image is synthesized by selecting from each of the 64 column-specific restorations the columns for which the proper antenna pattern was used. The computation time can be reduced with small increase in error if only 5 restorations are calculated corresponding to zones of columns instead of one restoration for each column.

Methods operating in the space domain, such as Backus-Gilbert or the ACLS filter, can be applied directly to the PMI case simply by varying the coefficients of the antenna pattern in the system of linear equations [Hunewinkel, 1993].

Sethmann *et al.* [1994] also point out that a necessary condition for image restoration is to sample the brightness temperature on earth close enough so that no aliasing in the frequency domain can occur. Or, stated in the space domain, the samples must not be independent but show a certain redundancy caused by the overlap of the integration regions of adjacent samples. In the case of PMI sensors, this low pass filtering is performed by the antenna gain function. Sethmann [1992] has quantified the necessary condition on the antenna pattern for no aliasing in terms of the noise temperatures and the maximum signal dynamic. He finds that, for the SSM/I, the necessary attenuation of the received signal at the Nyquist frequency (=sampling frequency/2) is approximately -50 dB. Examination of the measured antenna gain functions (data obtained from J. P. Hollinger, NRL) indicated that attenuation is sufficient to prevent aliasing only in the 19 GHz channels.

An analogous investigation for the planned sensor MIMR has been carried out here by modelling the antenna patterns as Gaussian functions, using the latest available design specifications for the sample spacing and beam widths of the various channels [ACRI, 1993]. The results indicate that the degree of aliasing expected at 90 GHz (worst case channel) is equivalent to that presently found in the 19 GHz channel of the SSM/I.

SSM/I restoration results

The ACLS and Wiener filter deconvolution techniques as well as the Backus-Gilbert method have been applied to SSM/I data obtained over western Europe in early February 1991. These data are from the data set used in the second Algorithm Intercomparison Project (AIP-2). (See Part 1 and [Allam *et al.*, 1993] for a description of the complete AIP-2 data set.) Three scenes were selected which showed distinct cloud frontal systems over ocean and land.

The original brightness temperature image and the restoration results for a scene imaged on 7 February 1991 are shown in Figure 2.5 for the 19H channel. All restorations enhance the weather effects over ocean, especially in the horizontally polarized channels, and the transition from land to ocean is steeper than in the original

Table 2.2: Resolution Improvements s_{rest} of SSM/I Images. a = measured 3 dB width, EFOV = 3 dB width according to Hollinger *et al.* [1987]

Channel	EFOV	Original	Wiener		ACLS		B–G	
		a	a	s_{rest}	a	s_{rest}	a	s_{rest}
Image of 3 Feb 1991. Along-scan profile								
19H	43	58	47	1.2	36	1.6	48	1.2
19V	43	60	49	1.2	45	1.3	51	1.2
22V	40	54	43	1.3	41	1.3	49	1.1
37H	28	46	36	1.3	33	1.4	46	1.0
37V	29	49	40	1.2	36	1.3	49	1.0
Image of 7 Feb 1991. Along-track profile								
19H	69	74	64	1.2	48	1.6	58	1.3
19V	69	72	59	1.2	46	1.6	60	1.2
22V	50	70	55	1.3	48	1.5	67	1.0
37H	37	50	41	1.2	30	1.7	50	1.0
37V	37	51	39	1.3	30	1.7	51	1.0

data. In the Wiener and ACLS restorations overshooting can be observed near the coastline. Here the land shows higher brightness temperatures (green) than further inland and the ocean appears colder (dark blue) than the high sea. Overshooting is particularly pronounced in the English Channel. Inland areas of the Wiener and Backus-Gilbert restorations appear to be more noisy than in the original, whereas in the ACLS restorations they appear smoothed. This is a consequence of the smoothing properties of this filter in low variance regions.

To quantify the resolution improvement, the steepness measure was calculated as described above from several steep edges (coastlines) in the original and in the restored images for two different scenes. Table 2.2 presents the results for all channels restored. Also shown in Table 2.2 are the 3 dB widths (EFOVs) as given in the SSM/I Users Guide [Hollinger *et al.*, 1987] and the 3 dB widths (a) obtained from the Gaussian fits to the profiles according to Eqn. 2.22. The ACLS filter yields the highest resolution improvement. As already noted, the ACLS filter is locally adaptive so that the resolutions calculated here are not valid in the whole image but specific to the considered edge. For edges of less contrast or regions of low standard deviation, the resolution improvement is smaller. The resolutions in the Backus-Gilbert restorations are nearly constant over all channels as the goal of this procedure is uniform resolution at all channels equivalent to that at 37 GHz. The results for this channel are simply copies of the original data, and the 85 GHz channels (not shown here) are smoothed down to the resolution of 37 GHz. According to the discussion of sampling rates and aliasing in the last section no attempt is made to restore the 85 GHz channels with the other restoration methods.

Evaluation in rain rate retrieval

To evaluate the resolution improved data they have been used in the rain rate algorithm developed by P. Bauer for rain retrievals over the ocean [Bauer and Schlüssel, 1993]. The ocean case was selected because the 85 GHz channel (needed for land retrievals; see Part 1) of the F8 instrument was not functioning at the time the AIP-2 data set was acquired. Also the antenna pattern information needed to restore the F10 data (which include the 85 GHz channel) is not available. The **bauer** algorithm for the case when no 85 GHz data are available is given by:

$$\begin{aligned} log_{10}(RR) &= 14.66 - (0.7448x10^{1}0)T_{19v}^{-4} \\ &- 0.04503T_{22v} + (0.5064x10^{5})T_{19h}^{-2} \\ &- (0.599x10^{5})T_{37h}^{-2} \\ &- (0.1172x10^{-3})(T_{37v} - T_{19h}) \end{aligned} \tag{2.23}$$

Figure 2.6 shows the results of rain rates derived from original and restored SSM/I images for 7 February 1991 using Eqn. 2.23. The rain rates derived with Wiener and ACLS restorations show more pronounced maxima in the rain fronts. The rainfield derived with the Backus-Gilbert results is more noisy than the others. This can be explained by the noisy character of the Backus-Gilbert restorations, which already has been observed in the inland regions.

Figure 2.2 shows scatterplots comparing the SSM/I-derived rain rates to those derived from FRONTIERS radar measurements on 7 February 1991. For this scene the Backus-Gilbert method produces the statistically best agreement as reflected in the regression line. Restoring the input data with the Wiener filter introduces more noise and actually reduces agreement relative to using the original data. Using data restored with the ACLS filter results in retrievals lying close to the 1-1 line of agreement. The bias and rms values given in the plots are based on rain rates $\geq$ 0.5mm/h as SSM/I retrievals below this value are unreliable [Bauer and Schlüssel, 1993].

Table 2.3 summarizes the bias and rms statistics for the three scenes analyzed. The bias varies considerably from one date to the next; the rms values are in general greater than the biases. This discrepancy between radar and SSM/I retrieval methods is attributed to the poor fit of the SSM/I algorithms to measurements over ocean in this region (see Part 1 on algorithm re-calibration). Therefore, the comparision is somewhat questionable. However, assuming that the trend if not the magnitude of the results is correct, Table 2.3 shows that except for the Wiener and Backus-Gilbert restorations of 7 February 1991 data, all restoration methods yield lower bias and rms values than the original brightness temperatures. In most cases retrievals using the ACLS and Wiener restorations yield very similar results: the bias and rms values are reduced by about 10 to 20 %. The exception is rain retrievals on 7 February 1991 where use of the Backus-Gilbert restoration data produces the lowest bias, and the ACLS data the lowest rms value.

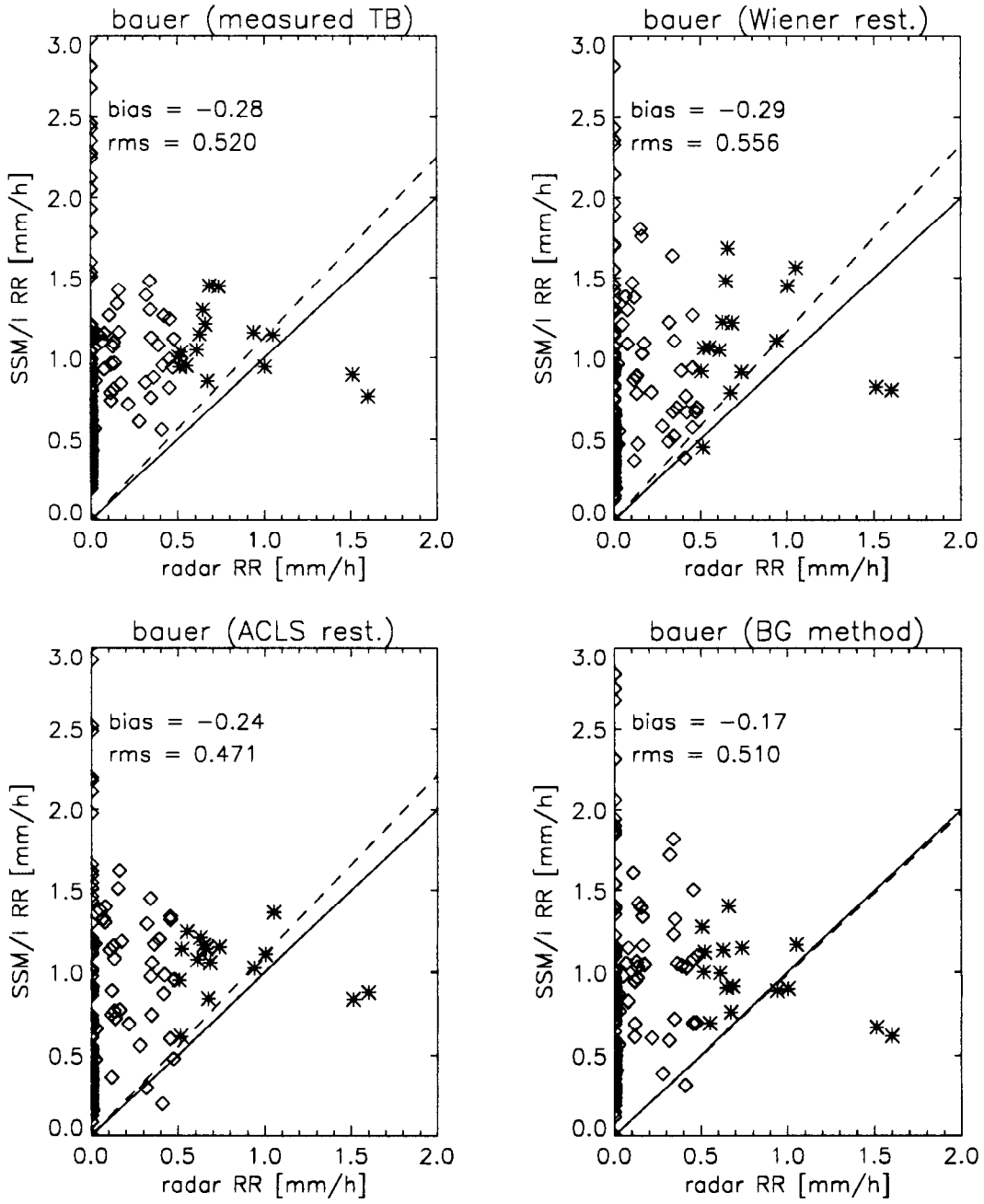

Figure 2.2: Scatterplots of SSM/I derived rain rates of 7 Feb 1991 vs. radar rain rates. Radar rain rates below 0.5mm/h are marked by a diamond and did not contribute to bias, rms and the dashed regression line.

Table 2.3: Comparision of SSM/I and radar rain retrievals.

SSM/I Restoration Algorithm	Date 3.2.1991		4.2.1991		7.2.1991	
	bias	rms	bias	rms	bias	rms
Number of samples $> 0.5mm/h$	13		30		16	
measured T_b	0.42	0.44	0.80	1.29	-0.28	0.52
ACLS	0.38	0.43	0.63	1.23	-0.24	0.47
Wiener	0.39	0.42	0.64	1.22	-0.39	0.56
Backus-Gilbert	0.43	0.44	0.75	1.24	-0.17	0.51

Conclusions

Five image restoration techniques were applied to test data in order to investigate their noise amplification and their resolution improvement charcteristics. A Landsat image was degraded using four different smoothing filters and three noise levels. Quantitative measures of performance including the normalized mean square error, noise amplification in spatial domain and the resolution improvement of sharp edges (steepness) were evaluated and compared. Due to its signal adaptive character, the adaptive constrained least squares (ACLS) method delivers restorations with the overall best results independent of the kind of degradation and noise in the data. The next best methods are the maximum entropy algorithm MemSys5 and the Wiener filter.

Application of these techniques to PMI data requires that the sampling geometry of the sensor be accounted for. Sampling and antenna pattern characteristics also have implications for successful image restoration. Examination of these characteristics for the SSM/I instrument revealed that the sampling theorem is fulfilled within the necessary approximation only for the 19 GHz channels. This means that restoring data from the higher frequency (higher resolution) channels would result in images with artefacts due to signal aliasing. An analogous investigation for the planned sensor MIMR was carried out by modelling the antenna patterns as Gaussian functions, using the latest available design specifications for the sample spacing and beam widths of the various channels. The results indicated that the degree of aliasing expected at 90 GHz (worst case channel) is equivalent to that presently found in the 19 GHz channel of the SSM/I. Based on our experience with restoring SSM/I data, it should be possible to successfully restore all MIMR channels, although some artefacts (for example overshooting at edges) may be present especially in the higher frequency channels.

Restorations of SSM/I images with the ACLS and Wiener filters were compared to those of the Backus-Gilbert method adapted to standardize the resolution in all channels. In all restorations image improvement is clearly visible; it is best when using the ACLS filter. Slight overshooting near coastlines is seen with the ACLS and Wiener filter restoration algorithms but not with the Backus-Gilbert method. However global restoration quality is only slightly influenced by single overshooting pixels.

Using the restored data in an algorithm for rain retrieval over the ocean improved agreement with coincident radar measurements, indicating that the beam-filling error can, at least partially, be compensated for using image restoration techniques. The results also indicate that restoring each channel to the highest resolution possible (as done with the ACLS filter) is more advantageous to rain retrieval than uniform resolution at all channels (as results from Backus-Gilbert deconvolution).

Further research in this area should include use of restored SSM/I data in regionally calibrated algorithms for rain retrieval over both ocean and land, and assessment of the theoretical restoration success with MIMR data through application of the Backus-Gilbert method to antenna pattern models.

References

ACRI, Optimisation of MIMR Data Acquisition Chain. ESA Technical Assistance Report, 1993.

Allam, R., G. Holpin, P. Jackson, and G.-L. Liberti, Second Algorithm Intercomparison Project of the Global Precipitation Climatology Project AIP-2. Pre-Workshop Report, 1993.

Backus, G., and F. Gilbert, Uniqueness in the inversion of inaccurate gross earth data. *Phil. Trans. Roy. Soc. London*, (A 266), 123–192, 1970.

Bauer, P., and P. Schlüssel, Rainfall, total water, ice water and water vapor over seas from polarized microwave simulations and Special Sensor MIcrowave/Imager data. *Journal of Geophysical research*, **98**, 20737–20759, 1993.

Bundschuh, B., Solution of ill posed problems by constrained minimization of an adaptively weighted smoothing function. In *Proc. IGARSS '91, Helsinki, Finland*, pages 305–308. IEEE Catalog No.91CH2971-0, 1991.

Farrar, M. R., and E. A. Smith, Spatial resolution enhancement of terresrial features using deconvolved SSM/I microwave brightness temperatures. *IEEE Trans. Geosci. Remote Sensing*, (GRS-30), 349–355, 1992.

Gonsalves, R. A., R. M. Korte, and J. P. Kennealy, Entropy-based image restoration: modifications and additional results. *Proc. SPIE*, **829**(Aications of Digital Image Processing X), 1987.

Gonsalves, R. A., and H. M. Kao, Entropy-based algorithm for reducing artifacts in image restoration. *Optical Engineering*, **26**(7), 617–622, 1987.

Gonzales, R. C., and R. E. Woods, *Digital Image Processing.* Addison Wesley, 1992.

Goodman, J. W., *Introduction to Fourier Optics.* McGraw-Hill, New York, 1968.

Gull, S. F., The Entropy of an Image. In Smith, C. R., editor, *Maximum Entropy and Bayesian Methods in inverse Problems*, Kluwer, Dordrecht, 1985.

Gull, S., Developments in Maximum Entropy Data Analysis. In Skilling, J., editor, *Maximum Entropy and Bayesian Methods*, Kluwer Academic Publisher, Dordrecht, 1989.

Hollinger, J., R. Lo, and G. Poe, *Special Sensor Microwave/Imager User's Guide.* Naval Research Laboratory, Washington, D. C., 1987.

Hollinger, J. P., J. L. Peirce, and G. A. Poe, SSM/I instrument evaluation, 1990.

Hunewinkel, T., Rekonstruktion von SSM/I-Daten mit einem adaptiven Least Squares Verfahren und der Maximum Entropie Methode. Master's thesis, Universiy of Bremen, 1993.

Jain, A. K., *Fundamentals of digital image processing.* Prentice Hall, Englewood Cliffs, 1989.

Jaynes, E. T., On the Rationale of Maximum Entropy Methods. *Proc. of IEEE*, **70**(9), 1982.

Lim, J. S., *Two-dimensional Signal and Image Processing.* Prentice Hall, Englewood Cliffs, 1990.

Poe, G. A., Optimum interpolation of imaging microwave radiometer data. *IEEE Trans. Geosci. Remote Sensing*, (GRS-28), 800–810, 1990.

Press, W. H., A. Teukolsky, W. T. Vetterling, and B. P. Flannery, *Numerical Recipes in C.* Cambridge University Press, Cambridge, 1992.

Robinson, W. D., C. Kummorow, and W. S. Olsen, A technique for enhancing and matching the resolution of microwave measurements from the SSM/I instrument. *IEEE Trans. Geosci. Remote Sensing*, (GRS-30), 419–429, 1992.

Sethmann, R., B. A. Burns, and G. Heygster, Spatial resolution improvement of SSM/I data with image restoration techniques. *IEE Trans. Geosci. Remote Sensing, in press*, 1994.

Sethmann, R., *Auflösungsverbesserung von SSM/I-Daten durch Bildrestaurationsverfahren.* PhD thesis, University of Bremen, 1992.

Short, D. A., and G. R. North, The beam filling error in the Nimbus 5 Electronically Scanning Microwave Radiometer observations of Global Atlantic Tropical Experiment rainfall. *J. Geophys. Res.*, **95**, 2187–2193, 1990.

Skilling, J., Algorithms and Aications. In Smith, C. R., editor, *Maximum Entropy and Bayesian Methods in inverse Problems*, Kluwer, Dordrecht, 1985.

Skilling, J., Classic Maximum Entropy. In Skilling, J., editor, *Maximum Entropy and Bayesian Methods*, Kluwer Academic Publisher, Dordrecht, 1989.

Skilling, J., Quantified Maximum Entropy. In Fourgere, P. F., editor, *Maximum Entropy and Bayesian Methods*, Kluwer Academic Publisher, Dordrecht, 1990.

Stogryn, A., Estimates of brightness temperatures from scanning radiometer data. *IEEE Trans. Antennas Propagat.*, (AP-26), 720–726, 1978.

Wahl, F., *Einfuehrung in die digitale Bildverarbeitung.* Springer Verlag, Berlin, 1989.

Figure 2.3: Test image for restoration methods.

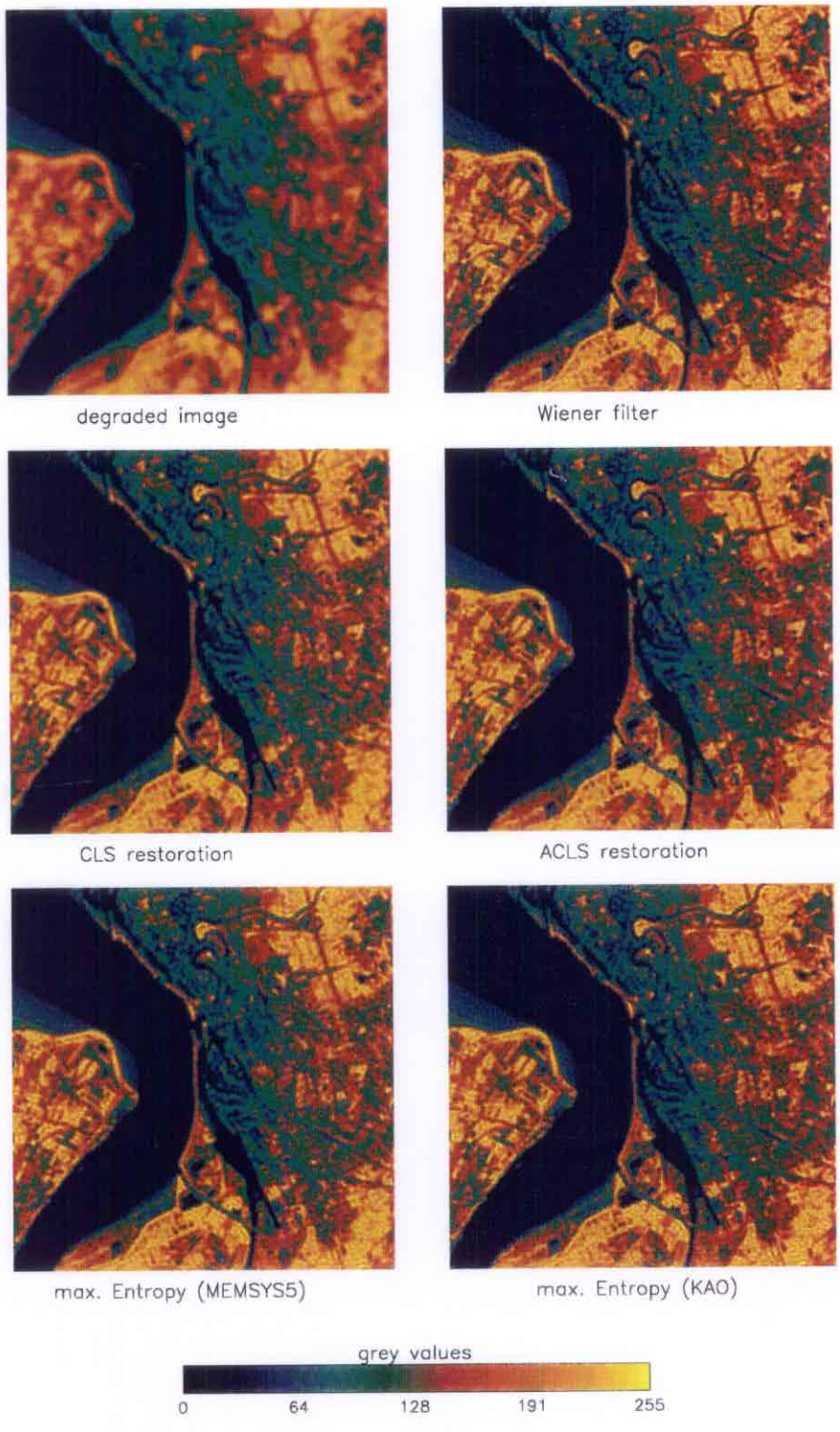

Figure 2.4: Bremerhaven Landsat scene, degraded with Gaussian low-pass ($\sigma = 2$) and Gaussian additive noise ($\sigma_n = 1$) and restoration results.

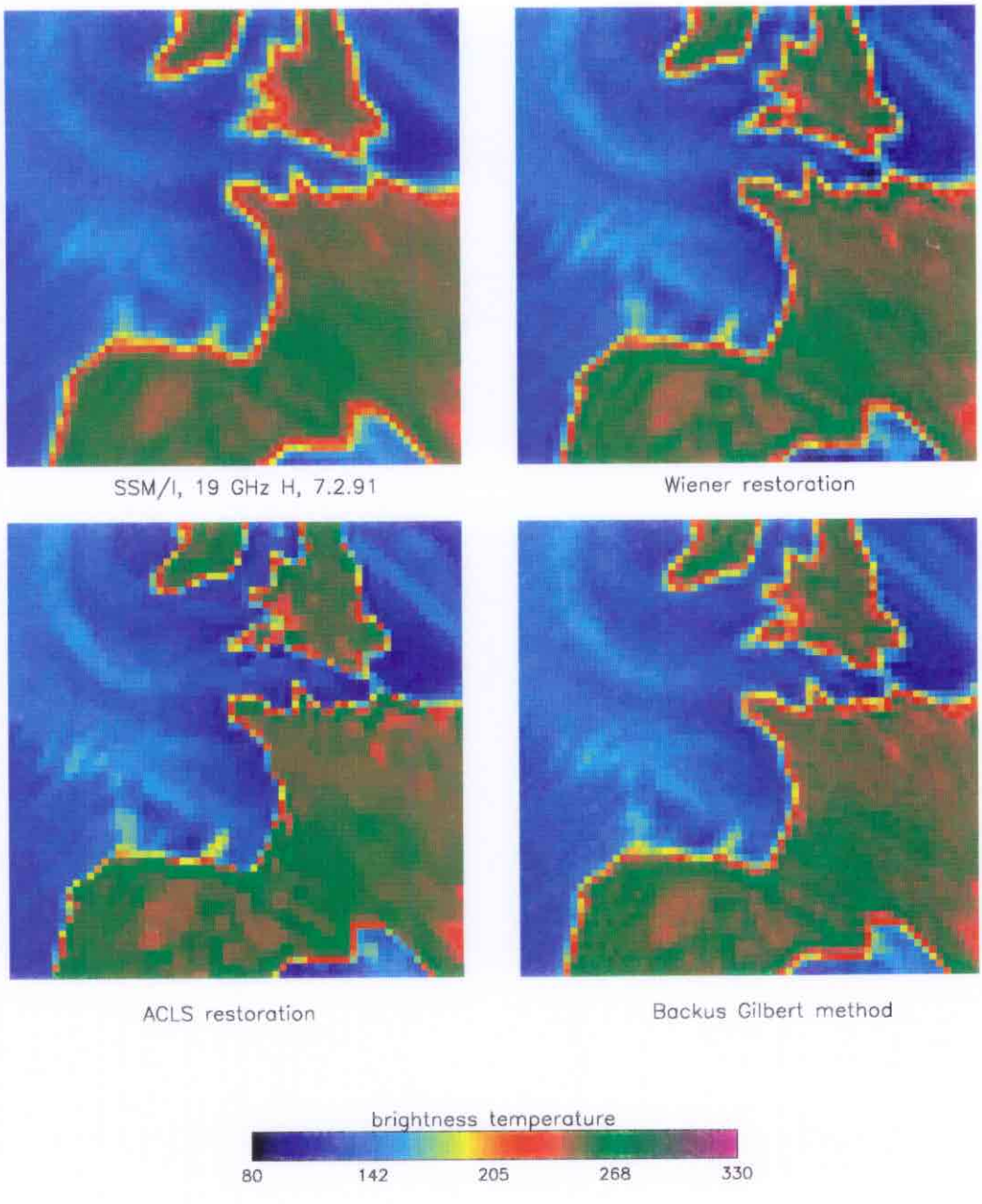

Figure 2.5: SSM/I 19 GHz H-Pol data of Europe: raw data and various restoration algorithm results.

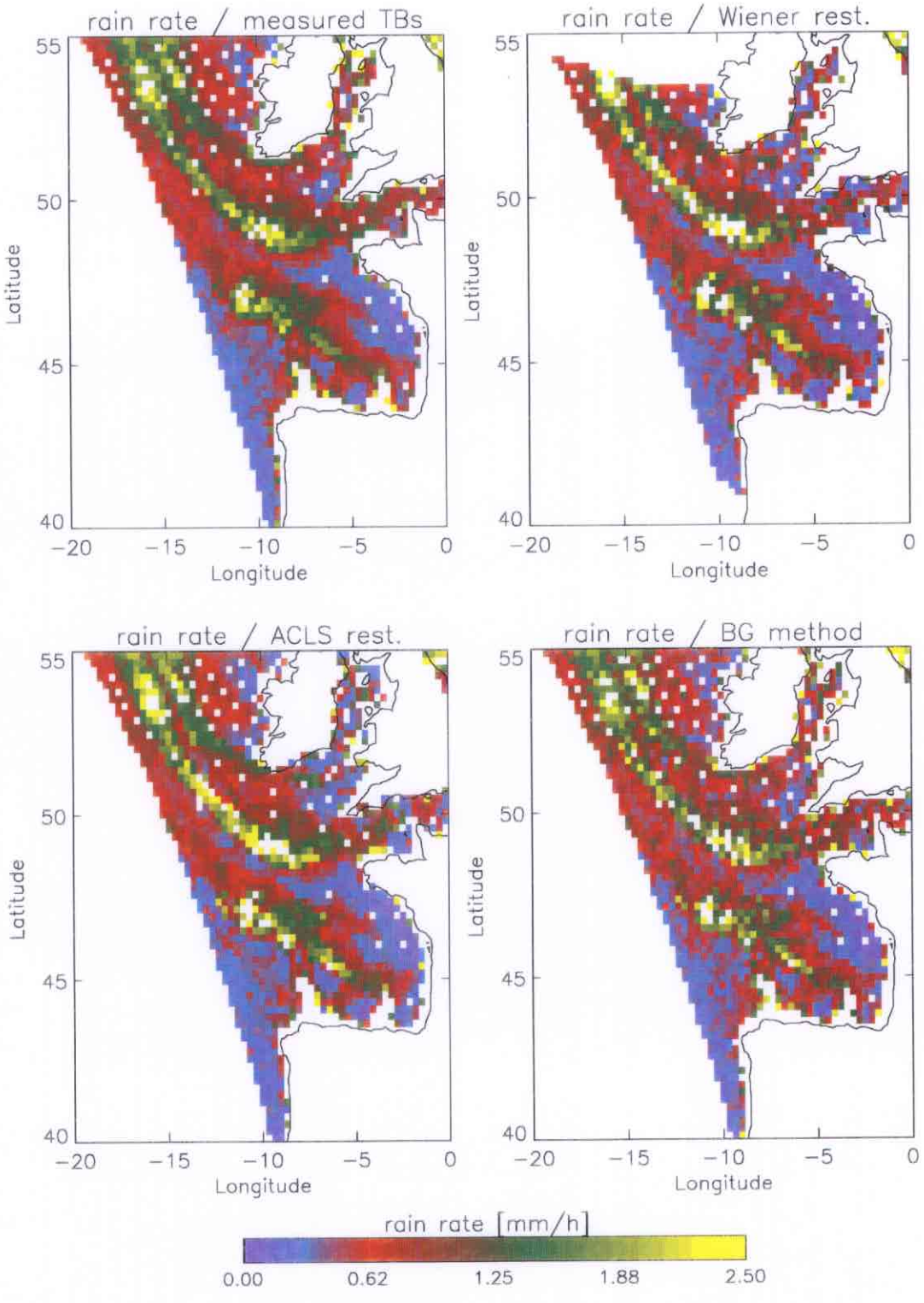

Figure 2.6: Rain rates over ocean on 7 Feb 1991 derived with SSM/I data using the **bauer** algorithm.